Environmental Science Nano

ROYAL SOCIETY OF CHEMISTRY

PAPER

View Article Online
View Journal | View Issue

Cite this: *Environ. Sci.: Nano*, 2026, **13**, 405

A Western-style diet shapes the gut and liver responses to low-dose, fit-for-purpose polystyrene nanoplastics in mice

Chloé Liebgott,[a] Melanie Mobley,[a] Sophie Miguel,[b] Valérie Bézirard,[a] Catherine Beaufrand,[a] Javier Jiménez-Lamana,[b] Rémi Dages,[a] Marie Tremblay-Franco,[a] Roselyne Gautier,[a] Jordan Denis,[c] Renaud Léonard,[c] Grégory Da Costa,[d] Catherine Robbe-Masselot,[c] Mathias Richard,[d] Cécile Canlet,[a] Bruno Grassl,[b] Stéphanie Reynaud,[b] Hervé Robert,[a] Hélène Eutamene[a] and Muriel Mercier-Bonin *[a]

Nanoplastics (NPLs) are an emerging global health concern, yet their toxicological impact remains uncertain, particularly among at-risk populations who are more susceptible to environmental stressors. While research on NPLs is expanding, most studies use commercial particles containing chemical additives, making it difficult to distinguish the effects of the polymer itself in its particulate form from those of confounding substances. In this study, we investigated the toxicity of fit-for-purpose, gold-labelled polystyrene NPLs (PS-NPLs; ~600 nm) in mice exposed *via* drinking water at literature-informed doses (0.1, 1, and 10 mg kg^{-1} per day) for 90 days, under either chow diet (CD) or Western diet (WD) conditions. Using ICP-MS, PS-NPLs were detected and quantified in intestinal contents. Moreover, low-dose exposure (0.1 or 1 mg kg^{-1} per day, depending on diet and endpoint considered) resulted in increased body weight gain, altered mucus quality (*i.e.* shift in mucin *O*-glycan profiles), and subtle impairment of gut barrier integrity in a diet-dependent manner. Low-dose exposure also altered the gut microbiota composition in both diet groups, with diet-specific profiles, and shifted caecal metabolomic signatures only in CD-fed mice. Metabolically, low-dose PS-NPL exposure exacerbated glucose intolerance in WD-fed mice and promoted hepatic lipid accumulation and a shift in droplet size, regardless of diet. Overall, these findings demonstrate that PS-NPLs, in their particulate form and in the absence of confounding additives, can induce non-monotonic, diet-modulated effects on the gut and liver. This highlights the importance of considering particle behaviour in complex biological environments and including both healthy and at-risk populations in NPL toxicity assessments.

Received 18th September 2025,
Accepted 11th November 2025

DOI: 10.1039/d5en00866b

rsc.li/es-nano

Environmental significance

Plastic pollution is a major and growing environmental and health concern, with increasing global production leading to the dissemination of plastic particles of various sizes, including nanoplastics (NPLs). Human exposure is now inevitable, and recent studies showing NPL detection in beverages and their migration from food-contact packaging highlight oral ingestion as a key route of exposure, with the intestine as the first organ exposed. Increasing evidence suggests that NPLs can induce intestinal and hepatic toxicity, raising concerns about long-term consequences for human health. Moreover, at-risk populations, such as individuals with metabolic disorders and/or dietary imbalances, may be particularly vulnerable. This study allows a better characterisation of the specific health impact of NPLs in their particulate form in both healthy and vulnerable populations, bridging environmental and human health issues.

Introduction

The exponential increase in global plastic production has led to plastic pollution emerging as a major environmental and public health concern. Worldwide, plastic production has increased from 1.5 million tonnes in the 1950s to 414 million tonnes in 2023.[1] Approximately 39% of total plastic production in Europe is dedicated to packaging applications,

[a] *Toxalim, Université de Toulouse, UMR INRAE 1331, 180 chemin de Tournefeuille, ENVT, EI-Purpan, BP 93173, 31027 Toulouse cedex 3, France.*
E-mail: muriel.mercier-bonin@inrae.fr; Tel: +33 (0)5 82 06 64 58
[b] *Université de Pau et des Pays de l'Adour, E2S UPPA, CNRS, IPREM UMR 5254, Pau, France*
[c] *Université de Lille, CNRS, UMR 8576-UGSF, Lille, France*
[d] *Université Paris-Saclay, INRAE, AgroParisTech, Micalis Institute, Jouy-en-Josas, France*

including food packaging. However, in the absence of effective management and recycling of plastic waste, there has been a pervasive accumulation of plastic debris across all environmental compartments.[2] Furthermore, the degradation of plastic debris over time leads to their fragmentation into smaller particles, including nanoplastics (NPLs), defined as plastic particles smaller than 1 μm in size and exhibiting colloidal properties.[3] Although the formation of NPLs through the fragmentation of plastic debris is well established, it is equally important to note that NPLs can also be released directly from consumer products, such as food contact articles during their use.[4] Items such as nylon tea bags, plastic rice cooking bags[5,6] and even plastic kitchen utensils can release substantial amounts of NPLs under normal usage conditions.[7] This highlights that in addition to environmental fragmentation, direct exposure to NPLs through the routine use of plastic-containing products constitutes a significant route of human ingestion.

Due to their small size and widespread dispersion, NPLs have been detected in various environmental matrices, including air,[8] water,[9] and soil.[10] More recently, they have also been found in food and beverages.[11] Consequently, from a toxicological perspective, oral exposure is a major route for NPLs, thus questioning their impact on gut health.[12] The gastrointestinal tract acts therefore as the first critical interface for their absorption and potential biological effects. Accordingly, due to their small size allowing them to easily cross biological barriers, investigating the impact of NPLs on intestinal barrier function and subsequent systemic translocation is of particular importance.

Studies in rodent models have demonstrated that exposure to NPLs can adversely affect intestinal health. Some studies have reported an accumulation of NPLs in the intestine.[13–16] Adverse effects have been reported, including reduced expression of tight junction genes,[17,18] alterations in mucus production and secretion,[15,19] and, in some cases, compromised tissue integrity associated to changes in crypt depth and villi length.[17,18,20–22] Additionally, several studies have reported changes in gut microbiota composition (*e.g.* alpha and beta diversity)[17,19,20] as well as signs of local inflammation.[18,20] Further research has linked perinatal exposure to NPLs to intestinal and metabolic alterations in adult offspring.[23] It is important to note that the observed effects are not restricted to the intestine; disruptions of the gut–liver axis have also been described, including the accumulation of lipids in the liver.[24–26]

Importantly, certain at-risk populations, such as individuals suffering from obesity, type 2 diabetes, inflammatory bowel disease (IBD), or other chronic illnesses, are suspected to be more vulnerable to the effects of NPLs.[27] Nevertheless, few studies have investigated the impact of NPL exposure in murine models that mimic these conditions, which are known to weaken the intestinal barrier.[28,29] Some studies have assessed the impact of NPLs in mice fed a high-fat diet (HFD) and revealed the synergistic effects of diet and NPL exposure. Li *et al.* administered 42 nm PS-NPLs intravenously (4–40 μg g^{-1} bw per day) for 3 or 15 days and reported increased hepatic lipid accumulation and inflammation compared with mice exposed to HFD alone.[30] Another study used 50–70 nm PS-NPLs in drinking water (0.02 or 2 mg kg^{-1} bw per day) for 8 days and found enhanced intestinal and hepatic inflammation under HFD conditions compared with HFD alone.[31] Similarly, Wang and co-workers administered 80 nm PS-NPLs *via* drinking water (1–30 mg kg^{-1} bw per day) over 8 weeks and observed glucose intolerance and hepatic lipid accumulation.[28] Taken together, these findings suggest that NPL exposure may have far-reaching consequences for gastrointestinal and systemic health, particularly in contexts that replicate real-life vulnerabilities.

However, the majority of the studies above have relied on commercially available NPLs, whose composition is frequently unknown (*e.g.* presence of chemical additives).[32] These studies therefore do not allow a distinction to be made between the potential toxicity arising from additives, the polymer itself, or a combination of the two.[33] To address these issues, we developed in the present study appropriate NPL models based on polystyrene (PS) that were synthesised through a controlled process and were free from potentially confounding additives. To track their fate and uptake *in vivo*, these NPL models were labelled in a stable and traceable manner, which is not always the case in published studies. More specifically, we employed a gold-core labelling strategy to enable high-sensitivity detection using inductively coupled plasma-mass spectrometry (ICP-MS).

Using these original fit-for-purpose NPL models, we investigated the effects of sub-chronic (90 days; 0.1, 1 or 10 mg kg^{-1} bw per day in drinking water) exposure in male mice fed either a standard chow diet (CD) or a high-fat/high-sugar Western-style diet (WD). The influence of this dietary pattern has never been addressed in the literature before. This study demonstrates how nutritional stress representative of modern Western dietary habits may influence the disruption of homeostasis in the gut and gut–liver axis in response to NPL exposure.

Experimental

NPL models: synthesis and characterisation

Gold-labelled PS-NPLs were produced *via* a three-step synthesis protocol. The first step consisted of synthesising gold nanoparticles (AuNPs) using the Turkevich method, which involves a rapid reduction reaction (10 min) of tetrachloroauric acid ($HAuCl_4$, 200 mL, 0.355 mM) at 100 °C by sodium citrate ($CtNa_3$, 3 mL, 39.4 mM). This redox reaction proceeds from Au(III) to Au(II) and ultimately to metallic Au(0), yielding a stable aqueous suspension of monodisperse AuNPs with an average diameter of 40 nm. In the second stage, AuNPs were encapsulated within a silica shell using a Stöber process. This silica coating was formed by hydrolysis and condensation of tetraethyl orthosilicate (TEOS, 0.3 mL, 4 mM) *via* a sol–gel reaction on the AuNPs

previously made (90 mL). The process took place in a water (22 mL)/isopropanol (224 mL) medium in the presence of ammonia (NH_3 25%, 8 mL, 0.3 M) at room temperature overnight under vigorous magnetic stirring. After purification by centrifugation (3 cycles of 10 min at 12 000*g*), the resulting gold–silica nanoparticles (Au–Si NPs) presented a mean diameter of 172 nm (Fig. S1A). The final step consisted of surface functionalisation and polymer coating. An organosilane coupling agent, 3-(trimethoxysilyl) propyl methacrylate (TPM, 290 μL, 11.3 mM), was grafted onto the surface of Au–Si NPs dispersed in 100 mL water/ethanol (20/80 (v/v)), with an inorganic particle solid content of 2.5 g L^{-1}, in the presence of ammonia (NH_3 25%, 1.93 mL, 0.278 M). The reaction mixture was stirred vigorously overnight at room temperature. Following purification by centrifugation (three cycles at 12 000*g* for 10 min), styrene emulsion polymerisation was initiated. This polymerisation step was conducted using the TPM-functionalised Au–Si NPs dispersed in 54.5 mL water/ethanol (20/80 (v/v)), with an inorganic particle solid content of 2.5 g L^{-1}. Degassed solutions of polyvinylpyrrolidone (PVP K-30, 3.5 mL, mass concentration of 0.06 g L^{-1}, 0.4% of the total mass), styrene (5.6 mL, 0.9 M) and potassium persulfate (KPS, 1 mL, 2 mM) were added to the dispersion at 70 °C under vigorous magnetic stirring and allowed to stand for 12 hours. After reaction, the solution was purified by five centrifugation cycles in water (10 min at 12 000*g*, 50 mL tubes, water is changed at each cycle in equivalent volume) until the supernatant conductivity dropped below 40 μS cm^{-1}. The plastic particles were stored in 3.4% solids (w/v) aqueous suspension. By using scanning electron microscopy (SEM), both the shape and size distribution of PS-NPLs were determined (based on the counting of 850 particles). Their hydrodynamic diameter and zeta potential were measured at 10 μg mL^{-1} by dynamic light scattering with a Zetasizer Nano ZS (Malvern Panalytical GmbH, Germany).

Experimental design

Six-week-old male C57BL/6J mice (weight 25.5 ± 1.3 g; Janvier Labs, France) were used in this study. They were kept in an animal facility under specific pathogen-free (SPF) conditions at a constant temperature (21 ± 2 °C) with a day per night cycle of 12 h and given free access to water and food (Harlan Teklad 2018, Envigo, USA). All mice were acclimated to standard housing for 14 days. The experiments were carried out according to the guidelines for care and use of laboratory animals laid down in European directive 2010/63/EU on the protection of animals used for scientific purposes and according to the ARRIVE guidelines. The experimental procedures and protocols were approved by the local Animal Ethics Committee of Toulouse Midi-Pyrénées and authorised by the French Ministry of Higher Education and Research under the reference APAFIS#43697-2023060108285710v3. As illustrated in Fig. 1A and in order to study the toxicity of a 90-day sub-chronic exposure scenario, mice were divided into distinct groups (n = 12 per group) for two series of experiments.

In a first series of experiments, mice were fed a standard chow diet (CD) (Harlan Teklad 2018, Envigo, USA) and randomly divided into 4 groups. Mice were exposed to PS-NPLs at a dose of 0.1 mg kg^{-1} bw per day (CD0.1), 1 mg kg^{-1} bw per day (CD1) or 10 mg kg^{-1} bw per day (CD10) in drinking water *versus* control animals, *i.e.* no PS-NPLs administered (CD0). In a second series of experiments, mice were fed CD or Western-style diet (WD) (U8955 version 19, SAFE®, France) and randomly divided into 5 groups. CD-fed mice were not exposed to PS-NPLs (CD0) and WD-fed mice

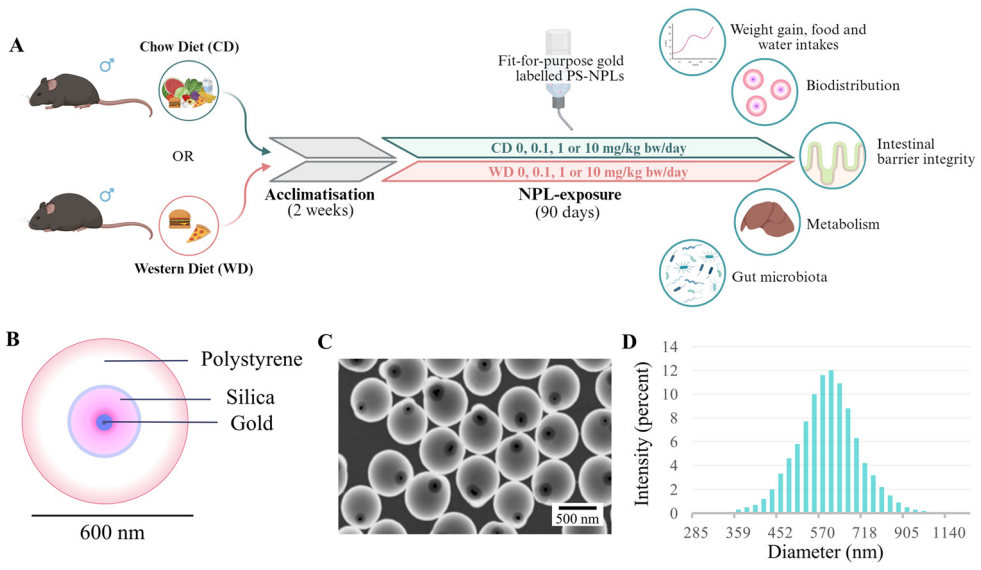

Fig. 1 Experimental exposure design and physicochemical properties of NPLs. (A) Schematic representation of the timeline of the experimental procedure. (B) Scheme of fit-for-purpose gold-labelled PS-NPLs. (C) Scanning electron microscopy (SEM) image of PS-NPLs. (D) Histogram of size distribution of PS-NPLs. Data are presented as the mean ± SEM.

were exposed to PS-NPLs at a dose of 0.1 mg kg^{-1} bw per day (WD0.1), 1 mg kg^{-1} bw per day (WD1) or 10 mg kg^{-1} bw per day (WD10) in drinking water *versus* control animals (WD0). To minimise plastic contamination from the laboratory environment, PS-NPLs were administered to mice *via* drinking water using glass feeding bottles equipped with metal teats.

Water intake by the animals was monitored daily throughout the exposure period in order to accurately calculate and control the actual dose of PS-NPLs administered. In addition, the concentration of PS-NPLs in the feeding bottles was adjusted during the experiment according to the weight gain of the animals.

Inductively coupled plasma-mass spectrometry (ICP-MS)

Thanks to the gold signature of the PS-NPL model, the biodistribution and quantification of PS-NPLs after 90 days of sub-chronic exposure were determined by using inductively coupled plasma-mass spectrometry (ICP-MS) in different digestive contents (stomach, small intestine, caecum and faeces), intestinal tissues (small intestine and colon) and organs (liver, spleen, testes, brain and kidneys). To this end, digestive contents, tissues and organs were collected and directly frozen in liquid nitrogen, then stored at −80 °C until analysis. The total gold content was determined by monitoring the isotope ^{197}Au with an Agilent 7900 ICPMS system (Agilent, Japan). The system consists of an integrated auto-sampler, a concentric nebuliser and a quartz cyclonic spray chamber as a sample introduction system. A calibration curve (0.1 μg L^{-1} to 10 μg L^{-1}) using a stock solution of ionic gold at 1000 mg L^{-1} (SCP Sciences, France) was prepared daily and the coefficient of determination R_2 was >0.99. Each sample was analysed in duplicate. Results are expressed as the mean of the two measurements. Prior to ICP-MS analyses, all samples were digested in aqua regia for 90 min at 90 °C in a heat block, then diluted with a 2% (v/v) HCl solution. The instrument limit of detection ($LOD_{(instrument)}$) and the limit of quantification ($LOQ_{(instrument)}$) are 11.8 and 36.7 ng Au per L, respectively. Quantification of PS-NPLs per gram of digestive contents was made possible thanks to single particle (SP) ICP-MS analysis (Fig. S1B), which provided the gold mass per single PS-NPL (0.92 fg Au/PS-NPL). Based on these data, an equivalent sample LOQ ($LOQ_{(sample)}$) was estimated by considering a 50 mg sample of digestive contents and averaging the calculated LOQ values across digestive contents, resulting in a value of 20.4 ng PS-NPLs per g dry mass.

Gene expression in the liver, jejunum and colon

RNA extraction and reverse transcription. Hepatic, jejunal and colonic pieces of tissue (30–50 mg) were isolated, immediately frozen in liquid nitrogen and stored at −80 °C until use. For RNA extraction, tissues were then homogenised in lysing beads matrix D tube (MP Biomedicals, Germany) with lysis buffer (guanidine isothiocyanate +1% β-mercaptoethanol) using a Precellys® evolution homogeniser (Bertin Technologies, France). The program included two 10 s cycles at 10 000 rpm, separated by a 10 min standby time in ice. The successive purification and centrifugation steps, comprising genomic DNA removal step with a gDNA eliminator spin column, were carried out in accordance with the recommendations of the Qiawave RNA plus Mini kit (Qiagen, France). The RNA quality and concentration were verified with a NanoPhotometer® N60 (Implen, Germany) to check the 260/280 nm and 260/230 nm ratios and with 1% agarose gel electrophoresis to examine the 28S and 18S RNA integrity. Reverse transcription of RNA (1 μg) into cDNA was performed using an IScript™ Reverse Transcription Supermix (Bio-Rad, USA) on a C1000 thermal cycler (Bio-Rad, USA) with the following program: 5 min at 25 °C, 20 min at 46 °C and 1 min at 95 °C. The cDNAs were diluted tenfold and stored at −80 °C before analysis.

Quantitative real-time PCR. Quantitative real-time PCR (qPCR) was performed using a QuantStudio™ 5 device (Applied Biosystems, Thermo Fisher Scientific, USA) in 384-well plates, with 1 μL of cDNA mixed with IQ SybrGreen Supermix (Bio-Rad, USA) and primers in a final volume of 5 μL. The sequences of the primers used are given in Table S1. Specific gene amplification was verified by evaluation of the PCR product melting curve and qPCR data were analysed with LinRegPCR v2016 software to get the starting concentration (N0) expressed in arbitrary fluorescence units per sample: N0 = threshold/Eff $mean^{Cq}$ (Eff mean: mean PCR efficiency; Cq: quantification cycle). The relative level of expression of the analysed gene was normalised using two reference genes: ribosomal protein lateral stalk subunit P0 (*RPLP0*) and hypoxanthine phosphoribosyltransferase (*Hprt*).

Faecal lysozyme activity and lipocalin-2 level

Faecal waters were prepared in 0.5 mL of phosphate-buffered saline (PBS) supplemented with a protease inhibitor cocktail (cOmplete™, Roche, Switzerland). Faeces (40–50 mg) were ground in tubes containing 5 mm glass beads (Sigma-Aldrich, USA) using FastPrep-24™ (MP Biomedicals, Germany) during 3 cycles of 30 s at 6 m s^{-1} with 1 min breaks. After centrifugation for 10 min at 12 000*g* at 4 °C, supernatants were collected and kept at −80 °C until use. Lysozyme enzymatic activity in faecal samples was assessed using an EnzChek™ Lysozyme Assay Kit (Invitrogen, Thermo Fisher Scientific, USA) and levels of lipocalin-2 (LCN-2) were measured using a mouse LCN-2 DuoSet ELISA Kit (R&D Systems, Bio-Techne, USA). Protein concentrations were determined colorimetrically using a Pierce™ BCA Protein Assay Kit (Pierce, Thermo Fisher Scientific, USA). Kits were used referring to supplier instructions and measurements were obtained on a SPARK® 10 M microplate reader (TECAN, Switzerland). All values were normalised according to total protein content.

Mucus thickness in the colon

Samples from faeces-containing distal colon were stored in Carnoy's fixative (60% (v/v) ethanol, 30% (v/v) chloroform, 10% (v/v) glacial acetic acid) overnight. Tissues were subsequently dehydrated using a Thermo Scientific™ Excelsior™ ES tissue processor (Thermo Fisher Scientific, USA) using the following sequential program: 2 × 60 min anhydrous ethanol, 2 × 60 min butanol, 480 min butanol and 3 × 80 min paraffin at 60 °C. Tissue samples were embedded in paraffin blocks using a HistoStar™ Embedding Workstation (Thermo Fisher Scientific, USA). 5 μm thick cross sections were prepared using a Microm™ HM 340E microtome (Thermo Fisher Scientific, USA) and deposited on slides (Thermo Scientific Menzel-Gläser Superfrost®, Thermo Fisher Scientific, USA). Sections were deparaffinised and stained with haematoxylin/eosin and Alcian blue, as previously described.[34] Samples were then mounted with Diamount mounting medium (DiaPath, Italy) and dried 12 h before first observations. A representative section per animal was analysed and images were obtained using a NanoZoomer HT slide scanner (TRIGenotoul Imaging Platform, INRAE Auzeville Campus) with a 200× magnification objective. Mucus thickness was measured all around the longitudinal section of the full distal colon with a 100 μm step (corresponding to approximately 60 measurements) using Fiji software.[35]

O-Glycosylation of mucins in the colon

Colonic mucosa was gently scraped and solubilised in an extraction buffer containing 4 M guanidine chloride, 5 mM EDTA, 10 mM benzamidine, 5 mM *N*-ethylmaleimide, 0.1 mg mL^{-1} trypsin inhibitor, and 1 mM phenylmethanesulfonyl fluoride. The mucin-rich solution was then subjected to isopycnic density-gradient ultracentrifugation (Beckman Coulter LE80K ultracentrifuge; 70.1 Ti rotor, 417 600*g*, 15 °C, 72 h). Fractions containing mucins were pooled, dialysed against water, and lyophilised. Purified mucins were subjected to β-elimination under reductive conditions (0.1 M NaOH or KOH, 1 M $NaBH_4$ or KBH_4, 24 h, 45 °C). The resulting oligosaccharide–alditol mixtures were purified using a cation exchange resin (Dowex 50 × 2, 200–400 mesh, H^+ form). Purified glycans were permethylated under anhydrous conditions using 200 μL dimethyl sulfoxide, 300 μL iodomethane, and freshly powdered NaOH for 2 h at room temperature. The reaction was stopped by adding 1 mL acetic acid (5% (v/v)), followed by further purification on a C18 Sep-Pak column (Oasis HLB, Waters, USA). Permethylated oligosaccharides were analysed by matrix-assisted laser desorption ionisation-time of flight (MALDI-TOF/TOF) mass spectrometry (Analyzer 4800, Applied Biosystems/MDS Sciex), using 2,5-dihydroxybenzoic acid (DHB) as matrix. Samples were dissolved in 50 : 50 methanol/water and spotted onto the MALDI target. *O*-Glycan profiles were expressed as the relative percentage of each oligosaccharide species, calculated from peak integration of the MS spectra.

Oral glucose tolerance test (OGTT)

OGTTs were performed in the second series of experiments in mice. Mice were fed a Western diet (WD) and fasted for 6 h during daylight. Oral gavage was performed with glucose (2 mg glucose per g of body weight). Blood glucose levels were monitored from tail vein blood using a glucose meter (Accu-Chek® Performa) at baseline (0 min), 15, 30, 60, 90, and 120 min after gavage.

Hepatic lipid accumulation

Liver samples were embedded in Neg-50™ Frozen Section Medium (Epredia, USA) and cryosectioned using a Leica CM1900 cryostat (Microm HM550, MM France). The chamber temperature was maintained at −17 °C, and the blade temperature at −11 °C. Three serial sections of 9 μm thickness were obtained, mounted on Superfrost™ glass slides (Thermo Scientific, USA), and air-dried for 1 h. Slides were then fixed in 4% (v/v) formaldehyde for 15 min, followed by a 20 s rinse in phosphate-buffered saline (PBS), and a second 20 s wash in 30% (v/v) isopropanol (Sigma-Aldrich, USA). Subsequently, the slides were incubated for 10 min in an oil red O solution (Sigma-Aldrich, USA) to stain the neutral lipids and briefly rinsed in 30% isopropanol for 35 s to remove the excess stain. Nuclear counterstaining was performed using Harris' haematoxylin (Sigma-Aldrich, USA) for 30 s, followed by a 10 min rinse under running tap water. Finally, slides were mounted with Aquatex® mounting medium and allowed to dry for one week. Stained slides were digitised using a NanoZoomer digital pathology scanner (Hamamatsu, Shizuoka, Japan) and visualised with the NDP.view2 software (Hamamatsu). Digital images were analysed using ImageJ software, incorporating the YIQ Color Transformer plugin (https://imagej.net/ij/plugins/color-transforms.html). For each slide, five representative fields were selected at ×20 magnification to reflect the overall tissue architecture. The images were processed using the YIQ transformation to enhance the detection of lipid droplets, allowing for accurate quantification of the lipid-stained area. This method made it possible to determine the percentage of area occupied by lipid droplets and to estimate their number and size in different size categories. Particular emphasis was placed on the 5–10 μm, 10–15 μm, and 15–30 μm categories.

Gut microbiota composition characterisation and statistical analysis

Bacterial and fungal gut microbiota were analysed using 16S rRNA gene and ITS2 amplicon sequencing, respectively. The genomic DNA present in the faeces was extracted as previously described.[36] The integrity and concentration of extracted DNA were verified by NanoDrop® spectrometry. Microbial diversity was determined for each sample by targeting part of ribosomal genes. A 16S rRNA gene fragment comprising V3 and V4 hypervariable regions was amplified using an optimised and standardised 16S-amplicon-library preparation protocol (@Bridge, INRAE, Jouy en Josas, France).

Briefly, 16S rRNA gene PCR was carried out using 5 ng of genomic DNA according to Metabiote® protocol (or maximal of DNA volume) instructions using 192 bar-coded primers at final concentrations of 0.2 μM and an annealing temperature of 50 °C for 30 cycles. A similar approach was performed for the fungal faecal microbiota using the primers ITS2 (sense) 5′-GTGARTCATCGAATCTTT-3′ and (antisense) 5′-GATATGCTTAA GTTCAGCGGGT-3′ (Metabiote® MiSeq Primers, GenoScreen, Lille, France). PCR products were cleaned with an Agencourt AMPure XP-PCR Purification system (Beckman Coulter, Brea, USA), quantified according to the manufacturer's protocol and multiplexed at equal concentrations. Sequencing was performed using a 250-bp paired-end sequencing protocol on the Illumina MiSeq platform (Illumina, San Diego, USA). For 16S, raw paired-end reads were subjected to the following process: (1) quality filtering with the PRINSEQ-lite PERL script[37] by truncation of bases from the 3′ end not with quality <30 based on the Phred algorithm, (2) paired-end read assembly using FLASH[38] with a minimum length overlap of 30 bases and 97% overlap identity and (3) the search and removal of both forward and reverse primer sequences using CutAdapt, with no mismatches allowed in primer sequences. Assembled sequences for which perfect forward and reverse primers were not found were eliminated. Chimera sequences were removed using VSEARCH and UCHIME.[39,40] Readings were grouped into amplicon sequence variants (ASVs) at 97% identity level using the Galaxy tool for 16S sequences.[41] Each OTU was assigned to a different taxonomic level (from phylum to species) using the Silva database and the RDP classifier for the bacterial microbiota.[42] For ITS sequences, the dedicated FROGS pipeline[41,43] for sequence quality control, filtering and affiliation of taxa with the UNITE ITS database (version 8_3)[44] was used. Statistical analysis of 16S and ITS sequence data from the microbial communities was performed using R software (R Core Team, 2015, R Foundation for Statistical Computing, Vienna, Austria). Alpha diversity was estimated using the Shannon index or the observed number of species. Beta diversity was measured by a Jaccard distance matrix and used to construct principal coordinate analysis (PCoA) plots. After rarefaction of all the sequences at equal sampling depths, abundances of all the families were calculated by aggregating the ASVs assigned to these families. The level of significance was set at a p-value <0.05. To identify bacterial and fungal taxa differentially represented among the studied groups at different taxonomic levels (genus or higher level), linear discriminant analysis coupled with effect size (LEfSe) was applied.[45]

NMR metabolomics on caecal contents

Caecal samples were freeze-dried and extracted as previously described[46] with some modifications. Sample aliquots of 5 mg were mixed with 500 μL of the extraction solvent (MeOH/H_2O; 2 : 1; v/v), vortexed for 10 min, and centrifuged (10 min, 4 °C, 15 000g). Supernatants were collected. The remaining pellets were extracted again with 500 μL of extraction solvent, vortexed for 10 min, re-centrifuged (10 min, 4 °C, 15 000g) and supernatants were collected. Supernatants obtained from the two runs of extraction were pooled and centrifuged (10 min, 4 °C, 15 000g). Supernatants were collected and dried under vacuum.

Dried residues were dissolved in 270 μL of a deuterated buffer (0.2 M potassium phosphate buffer, pH 7.0, prepared in deuterium oxide and containing an external reference (3-trimethylsilylpropionic acid; TSP) at 0.2 mM) for the proton NMR analysis. Samples were then vortexed and centrifuged (15 min, 4 °C, 2800g). Quality control (QC) samples were prepared with 20 μL of each sample. 200 μL of supernatants were transferred into 3 mm NMR tubes.

Proton NMR spectra were obtained at 300 K on a Bruker Avance III HD 600 MHz NMR spectrometer (Bruker Biospin, Germany), operating at 600.13 MHz for ^{1}H resonance frequency using an inverse detection 5 mm ^{1}H-^{13}C-^{15}N-^{31}P cryoprobe attached to a cryoplatform (the preamplifier unit). "Tuning" and "matching" of the probe, lock, shims tuning, pulse (90°) and gain computation are automatically performed for each sample. ^{1}H NMR spectra were obtained using the 1D NOESY experiment with presaturation for water suppression (noesypr1d), with a mixing time of 100 ms. A total of 256 transients were collected into 64k data points using a spectral width of 20 ppm, a relaxation delay of 5 s and an acquisition time of 2.72 s. Prior to Fourier-transform, an exponential line broadening function of 0.3 Hz was applied to the FID. All NMR spectra were phase- and baseline-corrected and referenced to the chemical shift of TSP (0 ppm) using Topspin (V3.2, Bruker Biospin, Germany).

NMR spectra were then divided into fixed-size buckets (0.01 ppm) between 10.0 and 0.5 ppm using the AMIX software (v3.9.15, Bruker), and area under the curve was calculated for each bucket (integration). The regions including residual water (5.2–4.4 ppm) were removed. Preprocessed data were then exported into Excel files. Multivariate and statistical analyses are detailed in the SI.

Statistical analysis

Data are expressed as the mean ± standard error of the mean (SEM). Statistical processing was performed using GraphPad Prism version 10.5.0 for Windows (GraphPad Software, USA). The homogeneity of variances (Bartlett's test) was verified to determine which analyses (parametric or non-parametric) were required. When the homogeneity of variances was validated, a one-way ANOVA was performed with a Tukey post-test. Otherwise, a Kruskal–Wallis test was carried out with a Dunn post-test. The differences were considered statistically significant for a p-value <0.05.

Results

PS-NPLs are sub-micrometric, gold-labelled and monodisperse

A fit-for-purpose gold-labelled PS-NPL model was used. As illustrated in Fig. 1B, PS-NPLs were synthesised by aqueous emulsion polymerisation of styrene onto a gold–silica

core–shell nanoparticles, enabling polystyrene grafting and allowing precise particle tracking within the organism. The thickness of the polystyrene layer was adjusted so that the presence of the gold core did not significantly affect the overall density of the final nanoplastics, ensuring that their density did not exceed that of bulk polystyrene by more than 10%. The size and morphology of the synthesised PS-NPLs were characterised by scanning electron microscopy (SEM) (Fig. 1C). The particles observed *via* electron microscopy exhibited a spherical morphology, with an average core diameter of 580 ± 6 nm (Fig. 1C and D). The presence of a gold core was confirmed in 94% of the PS-NPLs, with an average of one gold nanoparticle per PS-NPL. Dynamic light scattering (DLS) measurements showed a hydrodynamic diameter of 595 ± 8 nm and a low polydispersity index (PDI) of 0.076 ± 0.048. As expected, the hydrodynamic diameter measured by DLS was slightly larger than the size determined by electron microscopy due to the contribution of the solvation layer in the aqueous suspension. Furthermore, zeta potential analysis revealed that the PS-NPLs carried a negative surface charge (−31.9 ± 0.6 mV). The low PDI measured by DLS and the results of zeta potential corroborate the high colloidal stability of the PS-NPLs in aqueous dispersion, suggesting that they are likely to remain dispersed under exposure conditions, such as in bottled water experiments.

Low-dose PS-NPL exposure affects mice weight gain under both CD and WD conditions

As shown in Fig. 2, the weight gain of animals relative to their initial body weight was monitored throughout the exposure period (Fig. 2A and C for CD and WD conditions, respectively), and the final weight gain at the end of the exposure period was calculated (Fig. 2B and D for CD and WD conditions, respectively). Interestingly, for CD-fed mice, a trend towards increased weight gain was observed for NPL-exposed animals, particularly in the CD0.1 group compared to the CD0 control group (Fig. 2A), although this difference did not reach statistical significance, even after 90 days of exposure ($p = 0.0886$) (Fig. 2B).

Specifically, the mean weight gain in the CD0.1 group was 30.4 ± 1.9%, whereas it was 25.3 ± 1.5% in the CD0 group. Regarding the effect of NPL exposure on WD-fed mice, a significant increase in weight gain ($p < 0.05$) was observed in the WD1 group compared to the WD0 control group at the end of the exposure period (Fig. 2C and D). Interestingly, under both dietary models (CD or WD), this weight gain effect was not observed at the highest exposure dose (10 mg kg^{-1} bw per day). Importantly, the increased weight gain observed at the end of the exposure period could not be attributed to increased food intake, as no significant differences related to PS-NPL exposure were detected in food consumption under either dietary condition (Fig. 2E and F for CD and WD conditions, respectively). Similarly, water intake remained unchanged across groups and confirmed that the actual exposure doses were consistent with the theoretical doses (Table 1).

Biodistribution of PS-NPLs in the whole organism shows no evidence of translocation or systemic passage under both CD and WD conditions

To investigate the biodistribution of PS-NPLs following oral exposure, the amount of NPL per tissue was determined by ICP-MS thanks to the gold signature associated with our NPL models. Quantification of PS-NPLs per gram of tissue was made possible thanks to single particle (SP)-ICP-MS analysis (Fig. S1), which provided the gold mass per single PS-NPL (0.92 fg Au/PS-NPL). No PS-NPLs were detected in any organs or digestive contents at the lower exposure doses (0.1 and 1 mg kg^{-1} per day) under either dietary condition (CD and WD). PS-NPLs were only detected in the digestive contents throughout the digestive tract (stomach, small intestine, caecum and faeces) at the highest exposure dose under CD (Fig. 3A) or WD (Fig. 3B) conditions. No PS-NPLs were detected

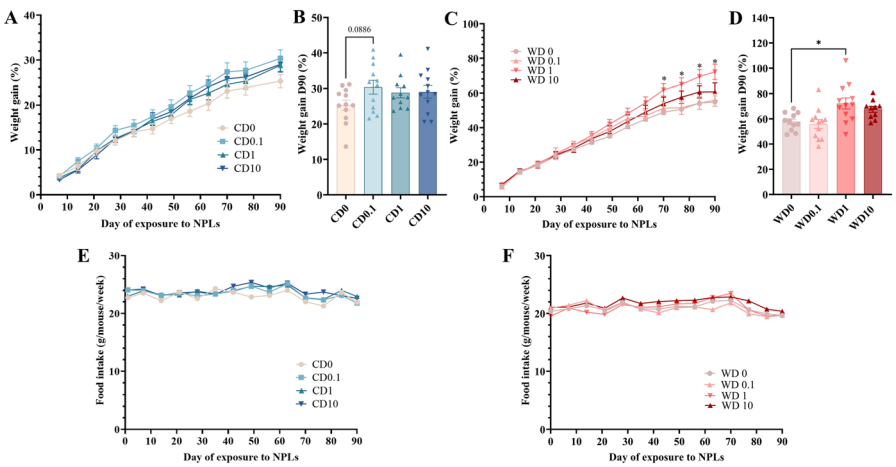

Fig. 2 Impact of PS-NPL exposure on the weight gain and food intake in mice under chow and Western diets. (A–D) Body weight gain in mice fed a chow diet (CD) (A and B) or a Western diet (WD) (C and D) during (A and C) and at the end of the exposure period (B and D). (E and F) Food intake in CD-fed (E) and WD-fed (F) mice throughout the exposure. Data are expressed as the mean ± SEM. $n = 12$ per group. *$p < 0.05$ *vs.* WD0 group.

Table 1 Water intake and actual exposure doses during the exposure period[a]

Group	PS-NPL concentration in feeding bottles (mg mL^{-1})	Water intake (mL per mouse per week)	Actual exposure dose (mg kg^{-1} bw per day)
CD0	0	30.4 ± 1.3	0
CD0.1	0.000625	29.5 ± 1.2	0.09 ± 0.01
CD1	0.00625	32.2 ± 1.5	0.99 ± 0.13
CD10	0.0625	32.1 ± 1.6	9.76 ± 0.89
WD0	0	27.9 ± 1.1	0
WD0.1	0.000625–0.001[a]	24.8 ± 0.6	0.08 ± 0.02
WD1	0.00625–0.01[a]	26.8 ± 0.8	0.87 ± 0.08
WD10	0.0625–0.1[a]	27.3 ± 0.8	8.90 ± 1.21

[a] PS-NPL concentration readjusted according to the weight gain of the WD-fed mice.

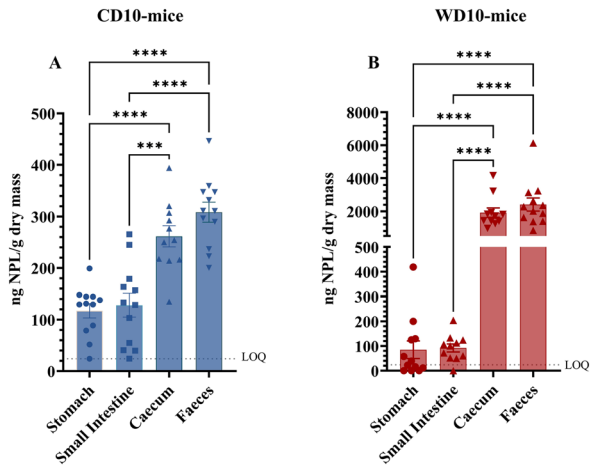

Fig. 3 Intra-luminal distribution of PS-NPLs throughout the gastrointestinal tract in mice exposed to the highest dose, as determined by ICP-MS analysis. (A and B) Biodistribution of NPLs in the intestinal content of CD10 (A) and WD (B) groups. $LOQ_{(sample)}$ = 20.4 ng PS-NPLs per g dry mass. Data are expressed as mean ± SEM; n = 12 per group. ***$p < 0.001$, ****$p < 0.0001$.

in intestinal tissues or peripheral organs analysed such as the brain, spleen, kidneys, liver, and testes (data not shown). It is worth noting that a significantly higher quantity of nanoplastics appeared to be detected in the caecum and faeces of exposed WD-fed mice compared to exposed CD-fed mice. Notably, a significantly greater quantity of nanoplastics was detected in the caecum and faeces of exposed mice fed the WD10 (1921.0 ± 284.4 ng PS-NPLs per g dry mass and 2412.0 ± 396.7 ng PS-NPLs per g dry mass, respectively) compared to those fed the CD (261.6 ± 20.60 ng PS-NPLs per g dry mass and 308.6 ± 19.546 ng PS-NPLs per g dry mass, respectively).

Low-dose PS-NPL exposure induces changes in tight junction-related gene expression in the jejunum without affecting overall gut permeability

In vivo intestinal permeability was not significantly altered following sub-chronic exposure to PS-NPLs for CD- and WD-fed mice whatever the dose administered (Fig. S2A and B, respectively). This finding is consistent with serum LBP levels, which also remained unchanged after exposure (Fig. S2C and D for CD and WD conditions, respectively). Despite there being no changes in functional parameters reflective of total gut paracellular permeability, alterations in the expression of tight junction genes in the jejunum were detected in animals exposed to PS-NPLs under both dietary conditions at the end of the exposure period. For CD-fed mice, in the lowest-dose group (CD0.1), a significant decrease in the expression of *ZO1* ($p < 0.05$; Fig. 4A), *JamA* ($p < 0.0001$; Fig. 4C), and *Cldn2* ($p < 0.05$; Fig. 4E) was observed. In WD-fed mice, changes in gene expression were also detected: *Cldn2* expression was altered at the lowest dose (WD0.1) ($p = 0.0759$; Fig. 2F), while a significant increase in *Cldn5* expression was noted in the WD1 group ($p < 0.05$; Fig. 2H). These findings suggest that while no measurable global changes in gut paracellular permeability were observed, PS-NPL exposure caused subtle local alterations at the intestinal epithelium cell level.

Low-dose PS-NPL exposure impairs colonic mucus quality without altering its quantity

To overcome the limitations of conventional mucus-related histological analyses, which often rely on single microscopic snapshots that may fail to capture the full heterogeneity of the colonic mucus barrier architecture, Kamphuis and colleagues[34] and later Gillois and colleagues[47] developed and optimised a method for such more comprehensive assessment. Building on this methodology, we investigated the faecal mucus layer in the distal colon, using representative longitudinal sections (Fig. 5A and C for CD and WD conditions, respectively). We quantified the average mucus thickness, and it remained unchanged across CD and WD conditions regardless of the dose administered (Fig. 5B and D, respectively). However, alterations in mucus-related gene expression were observed. Under CD conditions, PS-NPL exposure led to a significantly increased *Muc2* expression in the CD0.1 ($p < 0.01$) and CD10 ($p < 0.05$) groups compared to the CD0 group (Fig. 5G). In WD-fed mice, a significant increase ($p < 0.05$) in *Muc1* expression was observed in the WD0.1 and WD1 groups compared to the WD0 group (Fig. 5F). Similarly, a significantly increased expression of *Klf4* transcription factor, involved in goblet cell differentiation,[48] was observed in the WD0.1 ($p < 0.01$) and WD1 ($p < 0.05$) groups compared to the WD0 group (Fig. 5J). Although the coverage thickness of colonic mucus is essential, its 'quality', as determined by mucin *O*-glycosylation patterns, is equally critical. Therefore, we analysed and compared the abundance of neutral, sulphated, fucosylated and sialylated *O*-glycans in the colon of PS-NPL-exposed mice under both CD and WD conditions. In both CD- (Fig. 5K) and WD-fed (Fig. 5L) mice, only low-dose exposure (0.1 mg kg^{-1} bw per day) consistently triggered a twofold increase ($p < 0.001$) in mucin sialylation levels,

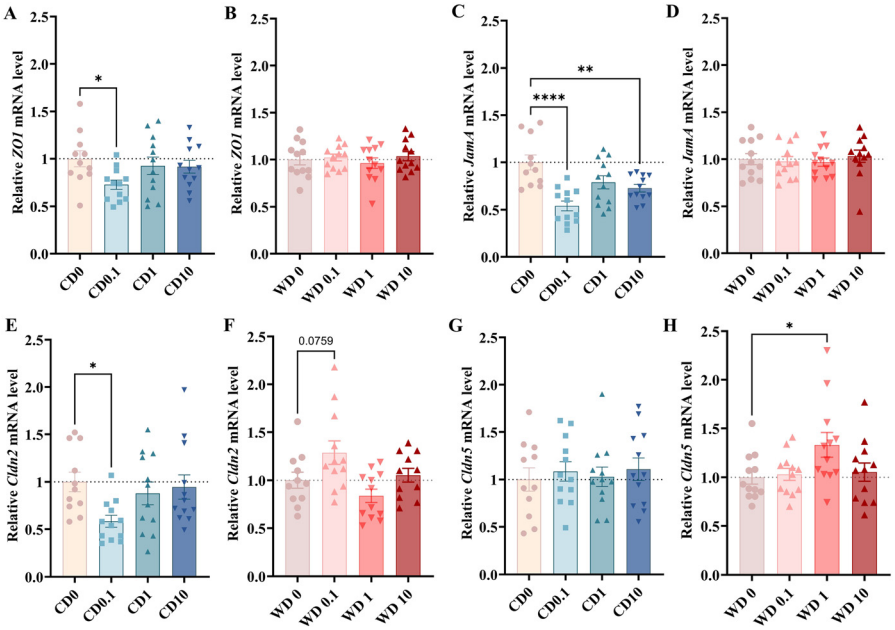

Fig. 4 Impact of PS-NPL exposure on tight junction gene expression in the jejunum according to the dose of exposure and dietary conditions. (A–H) Relative expression of tight junction genes compared to the CD0 or WD0 group. Data are expressed as the mean ± SEM. Values are normalised to the diet-matched control (CD0 or WD0). n = 12 per group. *$p < 0.05$, **$p < 0.01$, ****$p < 0.0001$ *vs.* respective CD0 or WD0 group.

concurrently with a reduction in neutral glycan content. These findings suggest a compensatory glycosylation response to PS-NPL exposure, which is possibly aimed at preserving barrier function under xenobiotic stress.

Low-dose PS-NPL exposure compromises colonic barrier defence, with effects modulated by dietary condition

As key indicators of mucosal antimicrobial defence and inflammation,[49,50] lysozyme and lipocalin-2 were jointly measured to further characterise colonic barrier integrity and its disruption in response to diet and/or PS-NPL exposure. First, *Lyz* gene expression was analysed in the colon of exposed mice at the end of the exposure period. Significant alterations were observed under both dietary conditions. A decrease in *Lyz* expression was detected in the CD0.1 ($p < 0.05$) and CD1 ($p < 0.001$) groups (Fig. 6A) compared to the CD0 group, whereas an increase was observed in the WD1 ($p < 0.05$) group (Fig. 6B) compared to the WD0 group. To determine whether these transcriptional changes had functional consequences, the faecal lysozyme enzymatic activity was measured.

Despite the dysregulation at the gene level, no significant changes in lysozyme activity were observed in the CD0.1 and CD1 groups (Fig. 6C). In contrast, a significant decrease in activity ($p < 0.05$) was detected in the WD groups, with a reduction of 47% and 41% in the WD1 and WD10 groups, respectively, compared to the WD0 group (Fig. 6D). These results suggest that PS-NPL exposure under nutritional stress conditions may impair the antimicrobial defence of the gut barrier. To complement these findings, the faecal concentration of lipocalin-2 was measured. A trend of decrease ($p = 0.0584$) was observed in the CD0.1 group compared to the CD0 group (Fig. 6E), whereas a significant increase ($p < 0.05$) was detected in the WD1 group relative to the WD0 group (Fig. 6F). Despite these alterations in faecal lysozyme and lipocalin-2, no significant changes were observed in faecal IgA levels (Fig. S3A and B). Similarly, the expression of pro-inflammatory cytokine genes such as *Tnfα* and *Il1β* remained unchanged by PS-NPL exposure (Fig. S3C–F). Nevertheless, these results collectively advocate that exposure to PS-NPL promotes colonic low-grade inflammation and alters the barrier defence mechanisms to some extent, depending on dietary condition.

Low-dose PS-NPL exposure alters glucose metabolism in WD-fed mice and induces hepatic lipid accumulation independently of dietary condition

In view of the well-established impact of WD on glucose intolerance[51] we focused our analysis on glucose metabolism using an oral glucose tolerance test (OGTT) specifically in WD-fed mice. Interestingly, exacerbated diet-induced glucose intolerance was significantly ($p < 0.05$) observed in the WD1 group compared to the WD0 group (Fig. 7A and B). Specifically, the area under the curve (AUC) increased by 17.5 ± 6.5% between the WD0 and WD1 groups, suggesting a synergistic effect between nutritional stress and PS-NPL exposure at this dose.

We next investigated the hepatotoxicity of PS-NPLs in mice under both diet conditions. Using Oil-red-O staining, we revealed an accumulation of lipid droplets in the liver due to PS-NPL exposure, as illustrated in the histological images (Fig. 7C–F), with a marked effect in the CD0.1 and

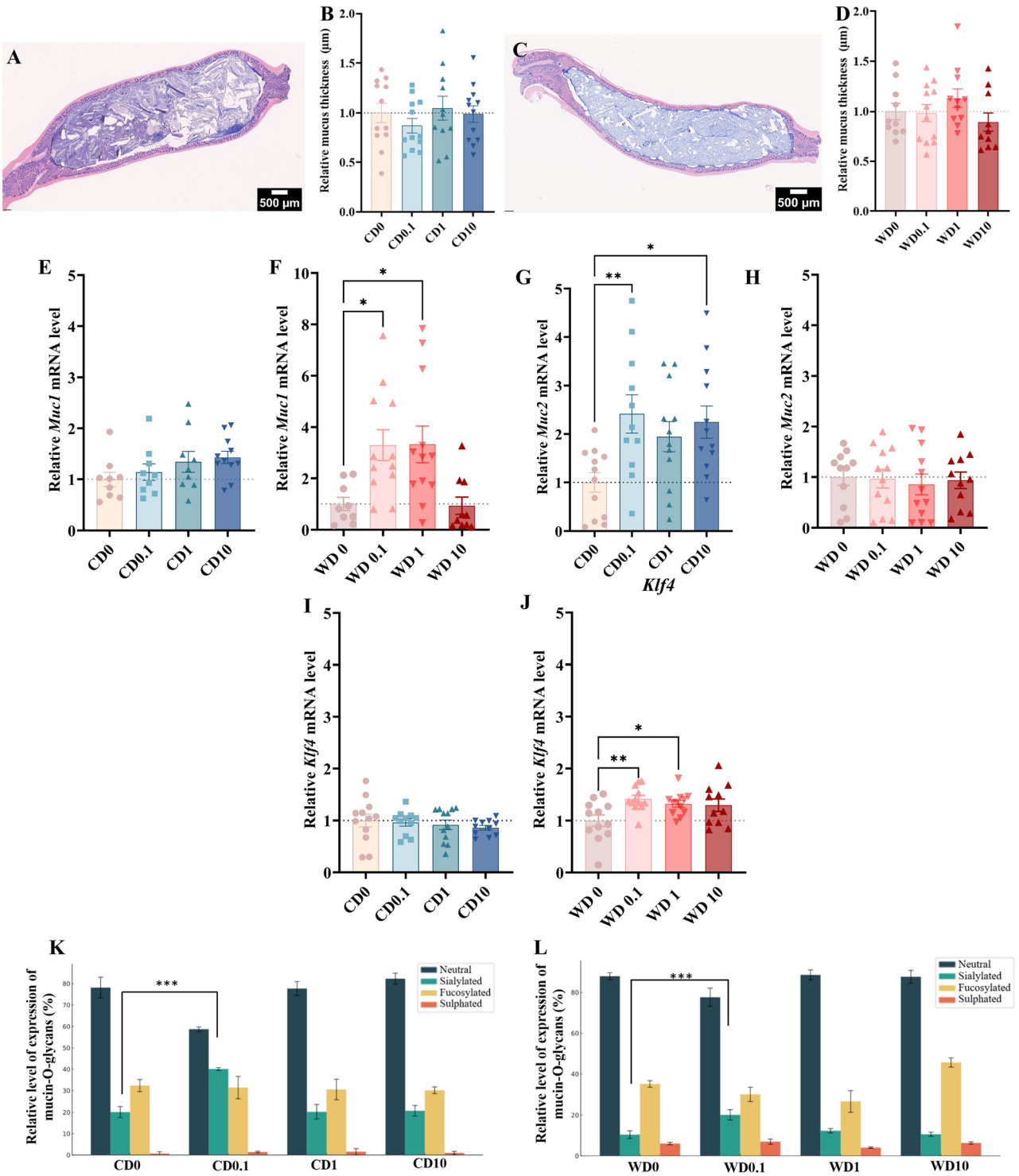

Fig. 5 Impact of PS-NPL exposure on colonic mucus at the end of the exposure period. (A and C) Representative Alcian blue-stained longitudinal sections of the colon from CD-fed (A) and WD-fed (C) mice. Mucus thickness for CD-fed (B) or WD-fed (D) mice, exposed to the three PS-NPL doses, compared to the CD0 or WD0 group. (E–J) Relative expression of mucus-related genes in the colon of CD-fed (E, G and I) or WD-fed (F, H and J) mice, exposed to the three PS-NPL doses, compared to the CD0 or WD0 group. (K–L) Relative level of expression of mucin-*O*-glycans in the colon of CD- (K) or WD-fed (L) mice. Data are expressed as the mean ± SEM. Values are normalised to the diet-matched control (CD0 or WD0). n = 12 per group. *$p < 0.05$, **$p < 0.01$, ***$p < 0.001$ *vs.* respective CD0 or WD0 group.

WD1 groups. In fact, the percentage of surface area occupied by lipid droplets was significantly increased ($p < 0.05$) in the CD0.1 group compared to the CD0 group, 1.0 ± 0.26% *vs.* 2.75 ± 0.54% of surface area, respectively (Fig. 7G). An increase in this percentage was also observed in the WD1 group compared to the WD0 group but without

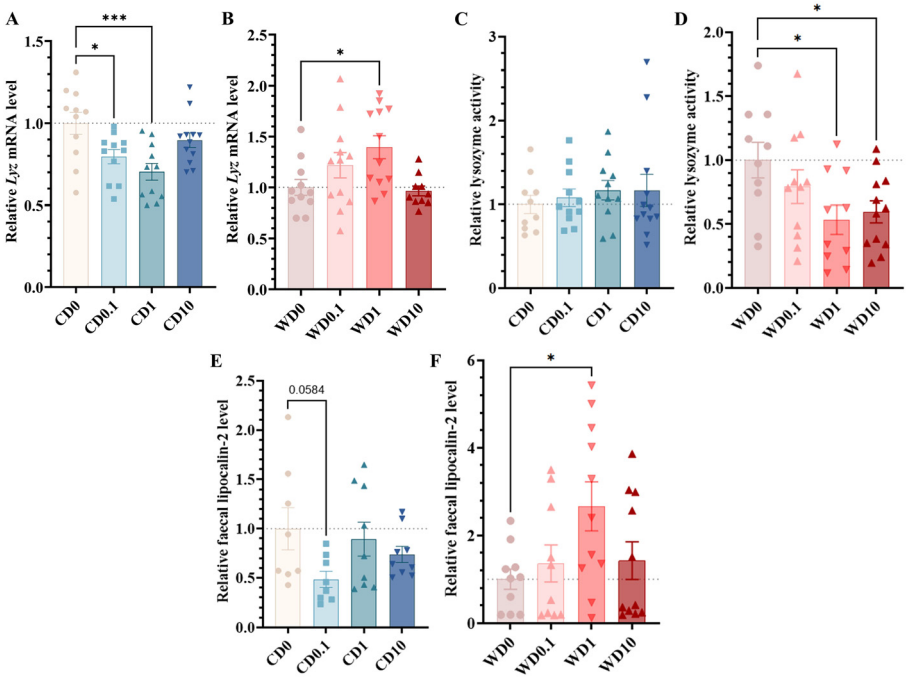

Fig. 6 Impact of PS-NPL exposure on colonic barrier defence in CD- and WD-fed mice: lysozyme gene expression, faecal lysozyme activity, and faecal lipocalin-2 levels at the end of the exposure period. (A and B) Relative expression of *Lyz* gene in the colon compared to CD0 (A) or WD0 (B) group. (C and D) Faecal lysozyme activity in CD-fed (C) and WD-fed (D) mice. (E and F) Faecal lipocalin-2 level in CD-fed (E) and WD-fed (F) mice. Data are expressed as the mean ± SEM. Values are normalised to the diet-matched control (CD0 or WD0). n = 12 per group. $*p < 0.05$, $***p < 0.001$ *vs.* respective CD0 or WD0 group.

reaching significance (21.4 ± 1.8% *vs.* 15.4 ± 3.0% of surface area; Fig. 7H).

In light of these findings, we further analysed the size distribution of lipid droplets (Fig. 7I) and then focused on three size categories, 5–10 μm, 10–15 μm and 15–30 μm. Interestingly, in the lowest dose group CD0.1, a significant increase in the proportion of lipid droplets sized 5–10 μm ($p < 0.05$) (Fig. 7J), 10–15 μm ($p < 0.05$) (Fig. 7L), and 15–30 μm ($p < 0.05$) (Fig. 7N) was observed. Similarly, in WD-fed mice, increases were noted in the proportions of 10–15 μm ($p < 0.05$) (Fig. 7M) and 15–30 μm lipid droplets ($p = 0.0767$) (Fig. 7O). These results demonstrate that PS-NPL exposure impacts hepatic lipid accumulation evidenced by an increase in droplet size. Biochemistry analysis was performed on plasma lipids, with cholesterol and triglyceride (TG) levels being measured. In CD-fed mice, a dose-dependent trend towards increased plasma TG levels was observed (Fig. S4A) as well as a trend towards increased cholesterol level ($p = 0.0845$) only at the lowest dose of exposure (CD0.1 group) (Fig. S4C) compared to the CD0 group. Concerning the WD-fed mice, a trend towards increased plasma TG levels ($p = 0.1192$) was observed only in the WD1 group.

At the molecular level, there was an up-regulation of the *Cd36* gene expression in the liver, involved in the lipid transport in the CD0.1 ($p < 0.01$) compared to the CD0 group (Fig. S4E). Of particular interest, there was also a significant increase in the expression of the *Cyp2b10* gene, involved in the metabolism of xenobiotics, in the CD0.1 ($p < 0.05$) and WD1 ($p < 0.01$) groups compared to the CD0 and WD0 groups, respectively (Fig. S4G and H, respectively). These findings further support the disruption of liver metabolic function after PS-NPL exposure, regardless of diet.

Low-dose PS-NPL exposure alters bacterial and fungal gut microbiota composition, with effects modulated by dietary condition

To examine the effects of PS-NPL exposure on the gut microbiota, we analysed modifications of the bacterial and fungal communities using 16S and ITS2 metabarcoding, respectively. A global analysis of bacterial and fungal microbiota at the different PS-NPL doses under either CD or WD showed significant effects only at the lowest dose: 0.1 mg kg^{-1} bw per day (Fig. 8, 9, S5 and S6).

Under CD condition, PS-NPL exposure strongly altered the bacterial microbiota. These changes were not visible at the phylum level (Fig. 8A) but both alpha and beta diversity showed significant differences between the CD0 group and the CD0.1group (Fig. 8B and C, respectively). Alpha diversity was clearly reduced in mice exposed to PS-NPLs, due partly to a decrease in total observed ASVs ($p = 0.054$), but also through more complex modifications of the ecological diversity, reflected by a significantly lower Shannon index ($p < 0.05$) in the CD0.1 group compared to the CD0 group (Fig. 8B). Beta-diversity PCA clustering confirmed that the microbiota was strongly influenced by

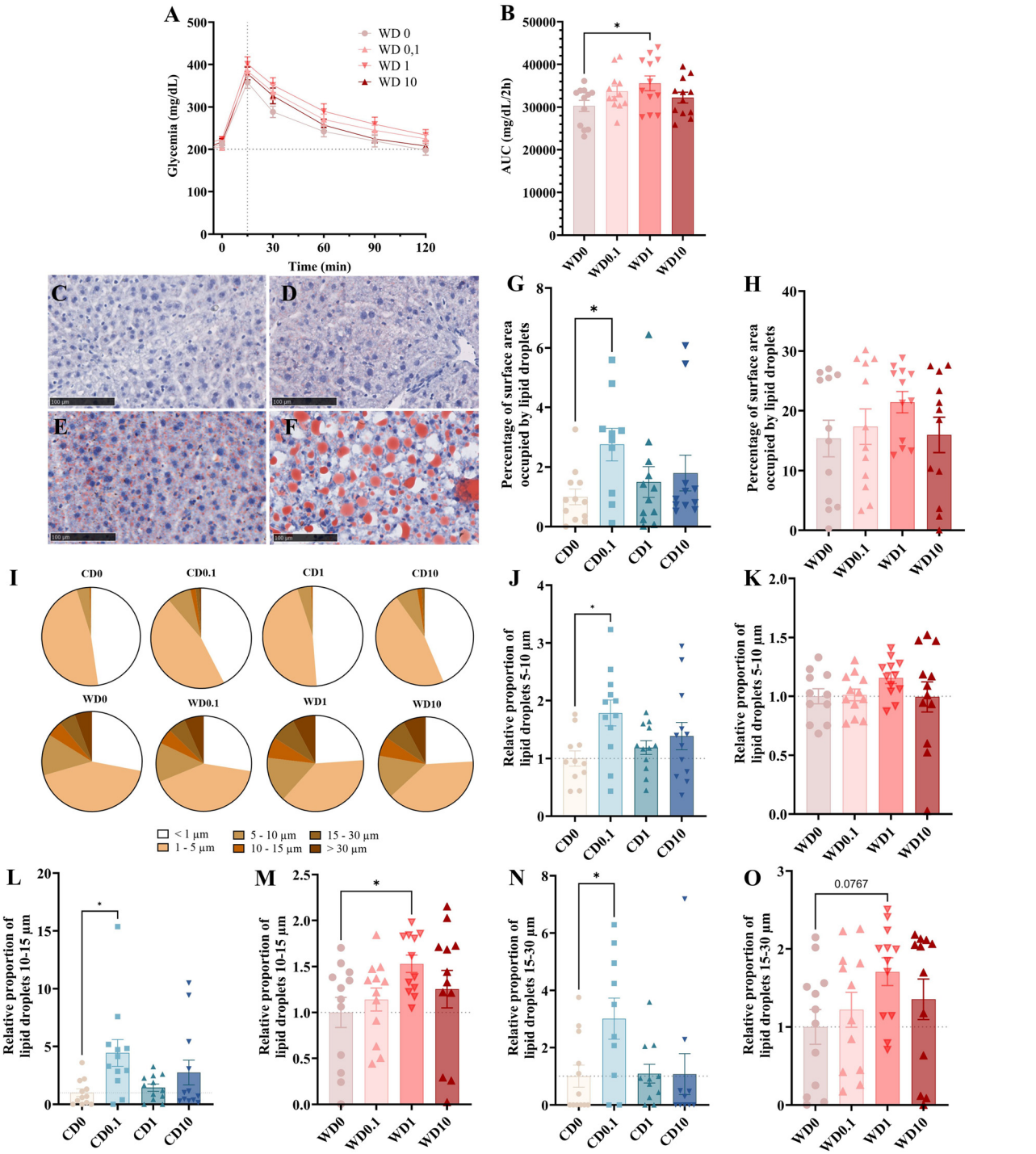

Fig. 7 Impact of PS-NPL exposure on glucose and lipid metabolism according to the dose of exposure and dietary conditions. (A and B) Blood glucose (mg dL^{-1}) from t = −30 min to t = 120 min after oral glucose gavage (t = 0 min), and the calculation of (B) area under the curve (AUC) of blood glucose 0–120 min (mg dL^{-1} min^{-1}) in WD-fed mice compared to the WD0 group. (C–F) Representative Oil red O-stained liver cross sections from CD0 (C), CD0.1 (D), WD0 (E) and WD1 (F) mice at the end of the exposure period. (G and H) Percentage of liver surface area occupied by lipid droplets in CD-fed (G) and WD-fed (H) mice. (I–O) Overall lipid droplet size distribution (I) and relative proportion of droplets measuring 5–10 µm (J and K), 10–15 µm (L and M), and 15–30 µm (N and O) in CD-fed and WD-fed mice compared to the CD0 and WD0 groups, respectively. Data are expressed as mean ± SEM. (J–O) Values are normalised to the diet-matched control (CD0 or WD0). n = 12 per group. *$p < 0.05$ *vs.* respective CD0 or WD0 group.

the PS-NPL exposure (p = 0.0019). To identify the specific taxa affected, we performed a differential analysis using the linear discriminant analysis effect size (LEfSe) bioinformatic tool. LEfSe identified a large number of

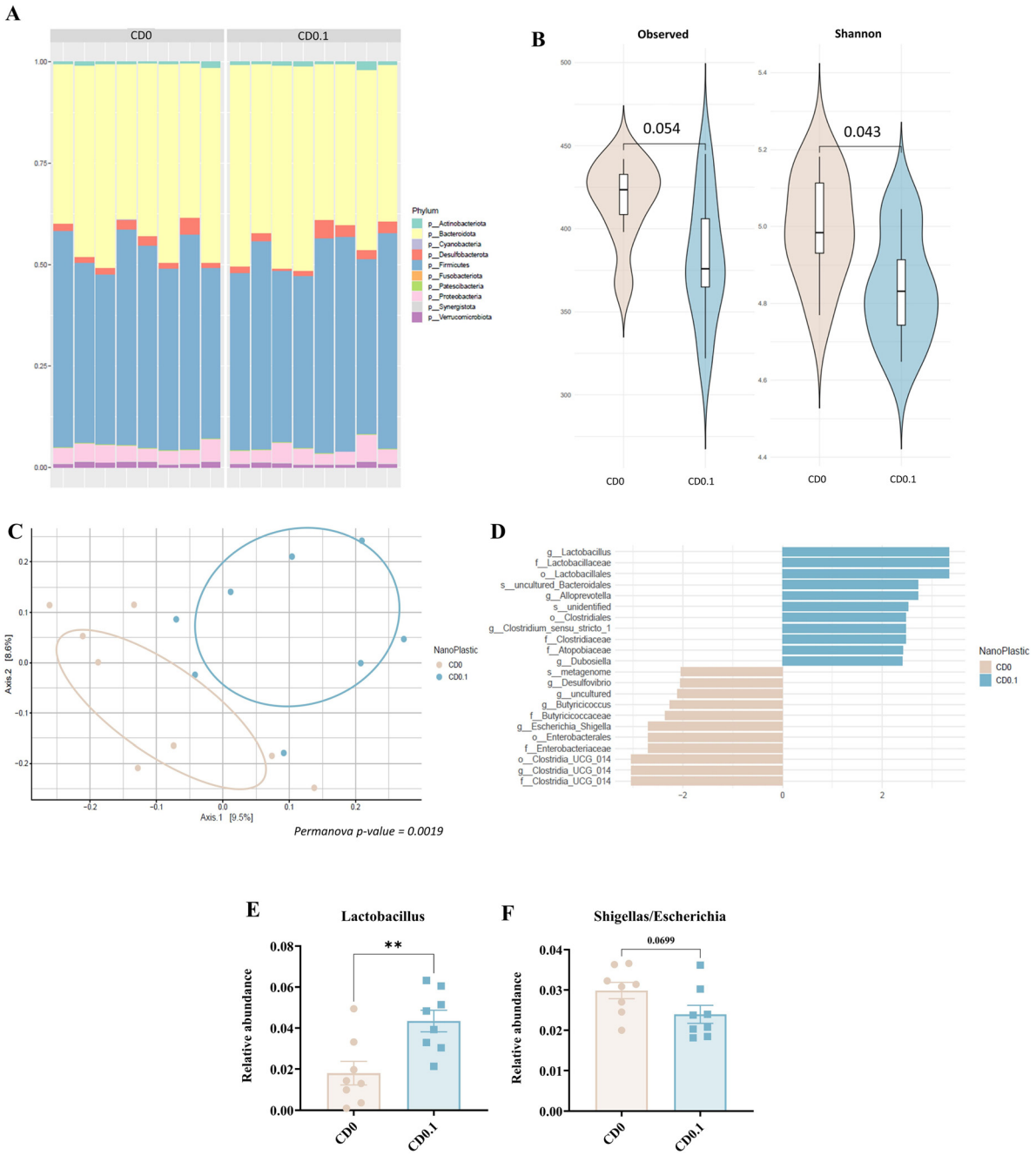

Fig. 8 Impact of low-dose PS-NPL exposure on the bacterial CD-fed mice gut composition. (A) Microbiota analysis at the phylum level in the faeces of CD0 and CD0.1 mice. (B) Observed richness and Shannon index describing the alpha diversity based on 16S, V3–V4 amplicon sequencing of the faecal bacterial microbiota of CD0.1 mice compared to CD0 mice. (C) Beta diversity illustrated by PCoA of Jaccard distance. (D) Overview of the relative abundance differences for selected taxa (orders, families and genera) in the faecal microbiota of CD0 and CD0.1 mice. (E and F) Differences in the relative abundance of selected bacterial genera in the faecal microbiota.

ASVs modified by PS-NPL exposure, including an increase in *Lactobacillus*, *Alloprevotella* and *Clostridium* genera in the CD0.1 group, while *Desulfovibrio*, *Butyricicoccus*, *Escherichia, Shigella* and *Clostridia*_CG_U14 decreased compared to the CD0 group (Fig. 8D–F). In contrast, fungal microbiota analysis in the same CD0.1 and CD0 samples (Fig. S5) showed very little measurable modifications following PS-NPL exposure with only a comparable decrease in alpha diversity quantified by the Shannon index (Fig. S5B; p = 0.0063), although no ASVs could be identified using LEfSe.

Under WD conditions, PS-NPL exposure did not affect the microbiota in the same way as under CD conditions (Fig. 9). However, the strongest effects were again observed in WD-fed mice exposed to PS-NPLs at 0.1 mg kg^{-1} bw per day (WD0.1 group). The reduction in alpha diversity observed in the CD0.1 group was here partly reproduced, but only in the

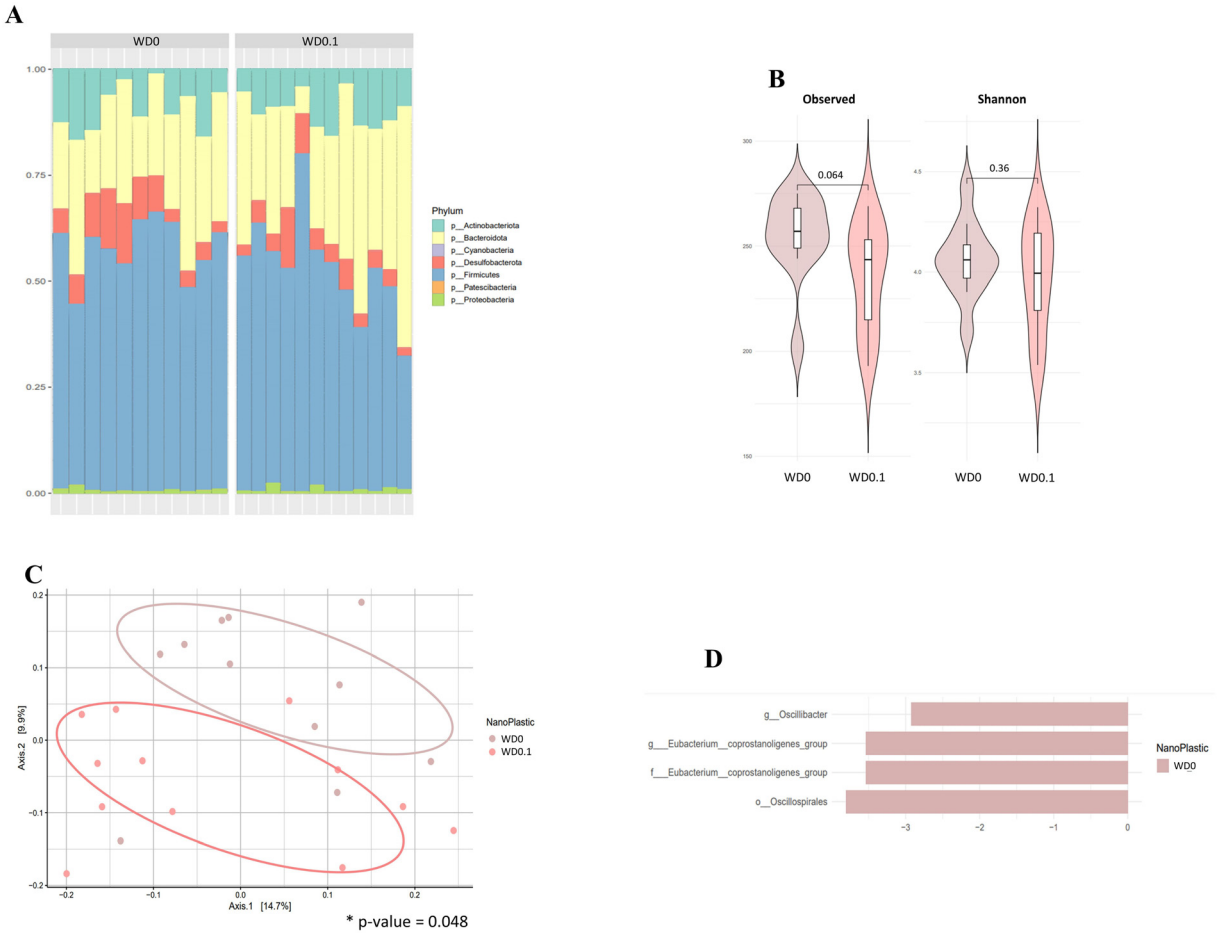

Fig. 9 Impact of low-dose PS-NPL exposure on the bacterial WD-fed mice gut composition. (A) Microbiota analysis at the phylum level in the faeces of WD0 and WD0.1 mice. (B) Observed richness and Shannon index describing the alpha diversity based on 16S, V3–V4 amplicon sequencing of the faecal bacterial microbiota of WD0.1 mice compared to WD0 mice. (C) Beta diversity illustrated by PCoA of Jaccard distance. (D) Overview of the relative abundance differences for selected taxa (orders, families and genera) in the faecal microbiota of WD0 and WD0.1 mice.

number of ASVs (Fig. 9B), while beta diversity showed a clear clustering (Fig. 9C). The LEfSe tool identified fewer discriminant ASVs, with the genera *Oscillibacter* and *Eubacterium* diminished following PS-NPL exposure (Fig. 9D). Fungal microbiota analysis under the same WD conditions showed a global modification of the phylum distribution, with an increase of *Basidiomycota* at the expense of *Ascomycota* (Fig. S6A). Although alpha diversity was unchanged (Fig. S6B), beta diversity PCA revealed significant clustering (Fig. S6C; $p = 0.01622$), suggesting specific modifications of ASVs. An increase in *Xylodon* and a decrease in *Samsoniella* following PS-NPL exposure were identified using LEfSe on the sequence data (Fig. S6D).

Low-dose PS-NPL exposure selectively alters caecal metabolomic profiles under CD conditions

In order to investigate the impact of PS-NPL exposure on microbiota features in more depth, we examined the caecal metabolic function by using proton NMR analysis under CD and WD conditions.

Firstly, PCA was applied to all observations. Under WD conditions, no significant or valid model was found for all exposure doses (data not shown). Under CD conditions, no discrimination between exposure doses was shown (Fig. 10A). No significant OPLS-DA model was fitted on these four conditions. Then, pairwise comparisons (between control and each exposure dose) were performed. No significant or valid model was found for the CD0/CD1 and CD0/CD10 comparisons.

A valid and robust OPLS-DA model with 1 predictive and 2 orthogonal components was constructed based on CD0 and CD0.1 group data. This model explained 79.4% of the variability ($R2$) and has a predictive ability value ($Q2$) of 0.455. Moreover, the p-value of the permutation test was equal to 0.01, validating the robustness of this model. The score plot is presented in Fig. 10B, showing a clear separation between the CD0 and the CD0.1 groups along the predictive component. 36 NMR variables were found discriminant (VIP $>$ 1.0) and significant (FDR-corrected p-value $\leq$ 0.05). These correspond to 10 metabolites. Intensity variation between CD0 and CD0.1 groups is

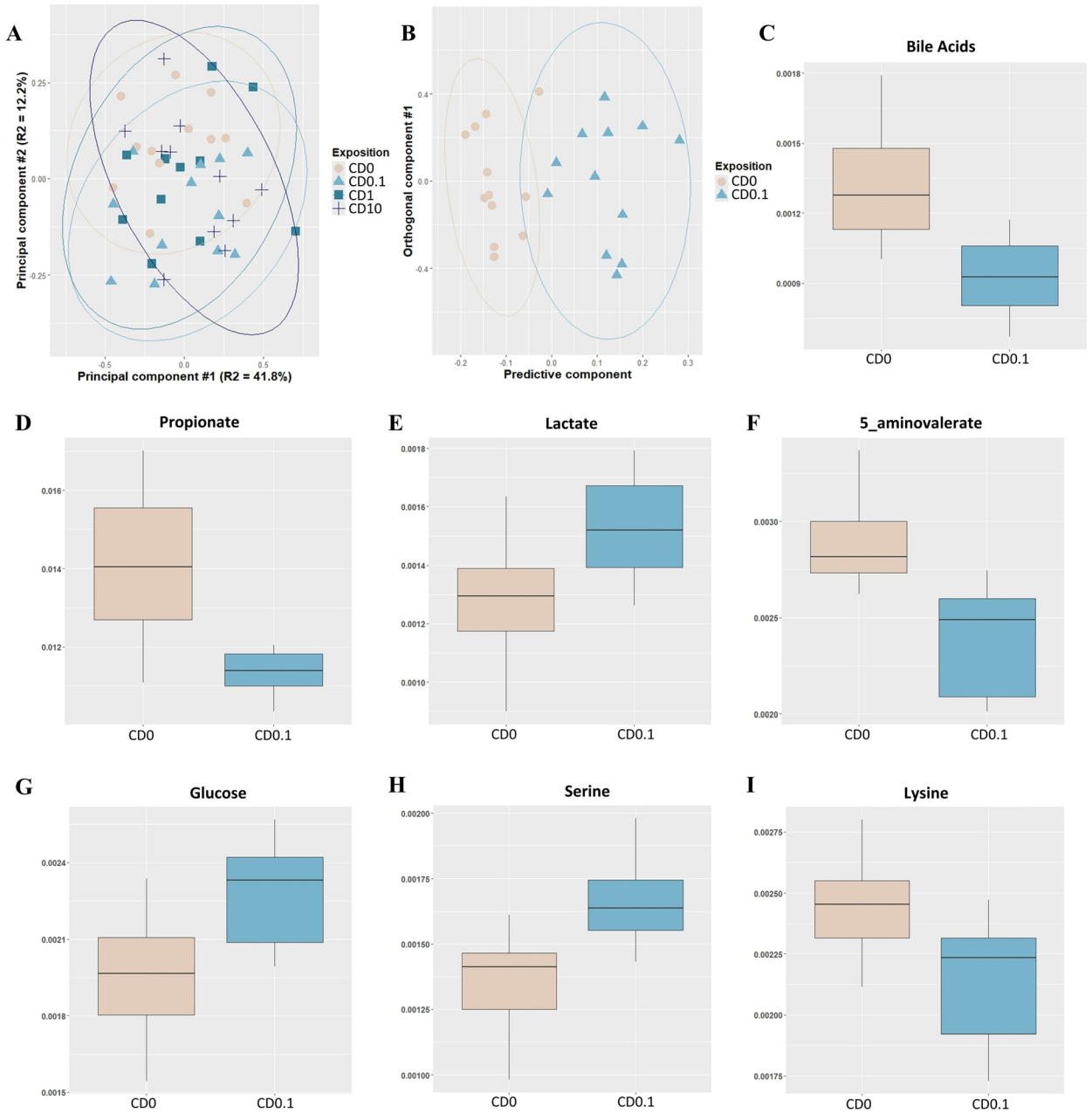

Fig. 10 NMR analysis of caecal content in CD-fed mice following exposure to PS-NPLs. (A) Two-dimensional PCA score plot of integrated ^{1}H NMR spectra of caecal extracts. Each symbol represents an observation (animal), projected onto first (horizontal axis) and second (vertical axis) principal components. Exposure doses are shown in different colours and shapes (control: light pink dots, n = 12; 0.1 mg kg^{-1} bw per day: pearl blue triangles, n = 12; 1 mg kg^{-1} bw per day: medium dark shade of cyan squares, n = 11; 10 mg kg^{-1} bw per day: navy crosses n = 11). The black ellipse determines the 95% confidence interval, which is drawn using Hotelling's T2 statistic. A = 2 principal components, $R2$ = 54.0%. (B) Two-dimensional OPLS-DA score plot of integrated ^{1}H NMR spectra of caecal extracts. Each symbol represents an observation (animal), projected onto first (horizontal axis) and second (vertical axis) principal components. Exposure dose *vs.* control is shown in different colours and shapes (control: light pink dots, n = 12; 0.1 mg kg^{-1} bw per day: pearl blue triangles, n = 12). The black ellipse determines the 95% confidence interval, which is drawn using Hotelling's T2 statistic. 1 predictive component, 2 orthogonal components, $R2$ = 79.4.0%, $Q2$ = 0.455, permutation p-value = 0.01. (C–I) Boxplot of intensities compared between the CD0 and the CD0.1 groups for metabolites found to be discriminant and significant following statistical analyses.

presented in Fig. 10C–I. A significant reduction in the intensities of bile acids (Fig. 10C), propionate (Fig. 10D), 5-aminovalerate (Fig. 10F) and lysine (Fig. 10I) was observed in the CD0.1 group compared to the CD0 group. Conversely, lactate (Fig. 10E), glucose (Fig. 10G) and serine (Fig. 10H) showed increased intensities following PS-NPL exposure at 0.1 mg kg^{-1} bw per day. These metabolomic alterations highlight the impact of even the lowest dose of NPLs on caecal metabolic profiles, suggesting disruptions to microbial activity in particular.

Discussion

Plastic pollution is now widely recognised as a global environmental and health concern. Numerous studies over the past decade have highlighted the toxicity of plastic debris to living organisms.[52] Nanoplastics (NPLs; <1 μm) are of particular concern due to their ability to cross biological barriers and reach systemic circulation. They have been detected in various dietary sources, including drinking water and beverages, raising questions about chronic oral exposure in the general population.[53] Since oral ingestion appears to be a major route of exposure to NPLs, the gastrointestinal tract constitutes the first barrier in contact with these particles.[12] Therefore, studying the effects of NPLs at the intestinal level is essential for understanding their potential impact on human health. In this study, we evaluated the effects of PS-NPL sub-chronic exposure (0.1, 1, and 10 mg kg^{-1} bw per day), consistent with literature-reported concentrations,[32] in C57BL/6 male mice over 90 days under standard chow (CD) or Western diet (WD) conditions. We focused on assessing the effects of these NPLs on intestinal barrier integrity, including mucus, and inflammatory response, gut microbiota composition, and hepatic responses, with a special emphasis on lipid accumulation.

An important asset of our study is the use of fit-for-purpose NPL models, synthesised *via* a controlled and additive-free process. Critically, the absence of additives or other plastic chemicals allows us to attribute any observed effects specifically to the polystyrene polymer itself in its particulate form, rather than to the potentially hazardous chemicals that are often present, albeit undisclosed, in commercial formulations.[32,33] Different strategies have been developed to detect and quantify NPLs in biological systems, including fluorescence, radiolabelling, and metal-tagging-based approaches. While fluorescence-based methods facilitate direct visualisation, they are prone to artefacts such as photobleaching, autofluorescence and dye leaching, which can compromise the accuracy of quantification.[32,54] Radiolabelling techniques, including the use of ^{89}Zr-labelled PS-NPLs[13] or radiolabelled monomers incorporated during polymerisation,[55] provide high sensitivity but may suffer from isotope leakage or require specialised radiochemical infrastructure. To further support our investigations that also aimed to define the biolocalisation of these particles in the body, NPLs were here labelled with a gold core, allowing high-resolution detection through inductively coupled plasma mass spectrometry (ICP-MS). To our knowledge, this is one of the first *in vivo* studies to use such controlled and traceable NPL models, providing a robust framework to assess specifically their host-material interactions. This study demonstrates that under physiological conditions and in the absence of any additional stressor beyond NPL exposure, PS-NPLs alone are sufficient to alter the intestinal barrier and the intestinal microbiota and induce hepatic effects, even without a pre-existing barrier dysfunction. To further investigate the impact of a known intestinal stressor, we also assessed the effects of PS-NPLs under a Western diet, which is well documented to impair gut barrier integrity.[51] The WD model was included to simulate nutritional stress closer to Western dietary habits and was validated by physiological, microbial and immune parameters (Fig. S7 and S8). As expected, WD0-fed mice gained significantly more weight than CD0 controls from week two ($p < 0.05$) (Fig. S7A) and showed impaired glucose tolerance ($p < 0.0001$) (OGTT, Fig. S7B and C). WD induced significant intestinal inflammation, evidenced by significantly increased faecal lipocalin-2 ($p < 0.01$) (Fig. S7D), elevated IgA levels ($p < 0.01$) (Fig. S7E), and higher faecal lysozyme activity ($p < 0.0001$) (Fig. S7F). WD also altered the mucus layer thickness ($p < 0.001$) (Fig. S7G), although intestinal permeability was only modestly affected (Fig. S7H–K). WD consumption significantly altered both bacterial and fungal microbiota, as evidenced by a consistent shift across all markers, with alpha and beta diversity indexes revealing a clear reduction in diversity and a marked clustering pattern (Fig. S8). Metabolomic analysis of caecal contents revealed clear separation between WD0 and CD0 groups, with altered levels of key microbial metabolites such as short-chain fatty acids (propionate, acetate, butyrate) known to be modulated by WD (Fig. S7L–O).[51] Hepatic changes included significantly increased liver lipid droplet area ($p < 0.0001$) and a shift across all droplet sizes ($p < 0.0001$ for 5–10 μm and 10–15 μm and $p < 0.001$ for 15–30 μm) for the W0 group compared to the CD0 group (Fig. S7P–S).

Biodistribution analysis using ICP-MS revealed that PS-NPLs were detected only in the intestinal contents of CD10 and WD10 mice (Fig. 3), with no measurable accumulation in analysed peripheral organs. The PS-NPL gold-labelling approach enabled highly sensitive and specific detection, with an instrument limit of quantification ($LOQ_{(instrument)}$) of 37 ng Au per L, which is comparable to that reported for palladium-doped PS-NPLs.[56] By coupling conventional ICP-MS with SP-ICP-MS (Fig. S1), elemental data could be converted into PS-NPL mass per gram of digestive content, allowing a direct estimation of the actual NPL load at different body locations and the calculation of an equivalent sample LOQ ($LOQ_{(sample)}$) of 20.4 ng PS-NPLs per g dry mass (for a 50 mg sample of digestive contents). This dual approach provides both elemental sensitivity and quantitative accuracy, strengthening the analytical reliability of NPL detection in our complex biological matrices. This $LOQ_{(sample)}$ value remains substantially lower than that reported in other studies on NPLs using advanced detection methods. For instance, Danquigny and colleagues reported higher LOQ in a study involving *Artemia* exposed to C13-labelled PS-NPLs.[57] The absence of measurable PS-NPL accumulation in peripheral organs (liver, spleen, kidneys, brain and testes) might suggest limited translocation across the gut barrier for both diet conditions. However, this possibility of translocation cannot be fully excluded. These results are

consistent with the unchanged *in vivo* gut permeability data obtained using FITC-dextran (Fig. S2) after PS-NPL exposure, although this marker reflects overall paracellular permeability. Notably, subtle modulation of tight junction gene expression was exclusively observed in the jejunum (Fig. 4), with no alteration in the colon (data not shown), suggesting segment-specific effects. Interestingly, PS-NPL levels in distal gut segments (caecum and faeces) were higher in the WD10 group than in the CD10 group. This observation could be explained by the increased intestinal transit time that is typically associated with nutritional stress models, which are known to prolong luminal retention due to low-fibre, high-fat/sugar content.[58] This could potentially lead to prolonged NPL retention within the gut lumen. These findings highlight how nutritional stress models, which are known to alter intestinal homeostasis, may influence the accumulation of NPLs within the gut and, subsequently, their biological impact.

We observed an increase in weight gain in mice exposed to low doses of PS-NPLs under both dietary conditions (CD0.1 and WD1), whereas this effect was not observed at higher doses (Fig. 2A–D). This non-monotonic response appeared across several biological endpoints, including modulation of tight junction gene expression occurring only in CD0.1, WD0.1 and WD1 groups (Fig. 4), a pattern that was mirrored in mucus-related gene expression (Fig. 5E–J) and mucin-*O*-glycans (Fig. 5K–L), lipocalin-2 level (Fig. 6E and F), and hepatic lipid droplet distribution (Fig. 7I–O). Disruption to glucose metabolism was specific to the WD1 group (Fig. 7B). The gut microbiota further reflected this non-monotonic pattern. Its composition showed distinct clustering of the CD0.1 (Fig. 8) and WD0.1 (Fig. 9) groups compared to CD0 and WD0, respectively. There were also differences in metabolic profiling between the CD0.1 and the CD0 groups (Fig. 10). Overall, the effects of PS-NPL exposure were predominantly observed at 0.1 mg kg^{-1} bw per day in CD-fed mice and 1 mg kg^{-1} bw per day in WD-fed mice.

It is important to emphasise that the non-monotonic response cannot be attributed to variations in water intake or taste aversion, as both water intake and actual exposure doses were monitored. A plausible explanation lies in the behaviour and physicochemical transformations of PS-NPLs within the digestive tract, including aggregation. While PS-NPLs remain dispersed in aqueous solutions due to their negative surface charge and electrostatic repulsion (Table 1), complex physicochemical conditions – such as electrolyte levels, pH, temperature, and dietary macromolecules like proteins and lipids – can disrupt this stability and promote aggregation.[59] The concentration of NPLs also plays a crucial role in aggregation dynamics. A study in saline medium showed that higher concentrations increase particle–particle interactions, favouring aggregation.[60] Consequently, the larger aggregates formed have a reduced surface area available for contact and are therefore less likely to interact intimately with the intestinal mucosa. In line with this, our study suggests that the highest doses (1 and 10 mg kg^{-1} bw per day, also depending on the diet) could generate larger PS-NPL aggregates that are more likely to pass through the gastrointestinal tract more rapidly. This results in limited contact and interaction with intestinal surfaces, which could lead to attenuated biological effects. While this is hypothetical, it aligns with literature showing that the size, shape and surface properties of micro- and nanoplastics govern their biological impact.[61,62] Importantly, the "critical" PS-NPL dose was influenced by the diet, as physiological effects were mainly observed at 0.1 mg kg^{-1} bw per day for CD and 1 mg kg^{-1} per day for WD. This may be due to interactions between PS-NPLs and the lipid-rich dietary matrix of WD. This dietary matrix can influence the aggregation properties of NPLs, the composition of their surface biocorona, and NPL–lipid interactions. Consequently, it can affect the threshold dose of PS-NPLs required to induce biological effects. Some studies have reported interactions of micro- and nanoplastics with lipids, potentially altering their physicochemical behaviour and biological effects.[63,64] Together, these findings emphasise the importance of considering not only the dose of NPLs administered but also their physicochemical transformations within complex biological and nutritional contexts in order to fully understand their bioavailability and toxicological potential.

Tang and colleagues reported a non-monotonic response to NPL exposure on body weight, with a significant increase observed in the lowest-dose group (2 mg kg^{-1} bw per day), and not at higher doses (10 or 50 mg kg^{-1} bw per day).[23] However, no explanation for this low-dose effect was provided by the authors. This was accompanied by the upregulation of lipogenic genes such as *Cd36*, suggesting that enhanced lipid biosynthesis might underlie the observed weight gain. Lu and colleagues also showed that chronic exposure to 100 nm PS-NPLs (0.1 g kg^{-1} food for 180 days) resulted in increased weight gain, hepatic lipid accumulation and elevated triglyceride levels.[65]

In addition to weight-related outcomes, metabolic disturbances have been reported. For example, Okamura and colleagues demonstrated that mice exposed to PS-NPLs (450–530 nm) in a high-fat diet (HFD) context developed glucose intolerance, as shown by iPGTT, along with increased expression of *Sglt1* in the small intestine.[66] These findings suggest that PS-NPLs may disrupt intestinal glucose handling in the context of HFD. Notably, glucose intolerance – also observed in our study – is an established early marker of susceptibility to type 2 diabetes, reinforcing the metabolic relevance of PS-NPL exposure under nutritional stress.[67] In parallel, these animals exhibited marked hepatic lipid accumulation under both control and HFD conditions.[66] These findings are in line with our study, in which low-dose PS-NPL exposure induced increased body weight under both CD and WD conditions, together with glucose intolerance and elevated hepatic *Cd36* expression specifically under WD. This reinforces the relevance of considering non-monotonic dose–response relationships when evaluating NPL toxicity. In addition to metabolic changes following PS-NPL exposure, we

noted disruptions to hepatic lipid metabolism. This was demonstrated by a greater proportion of liver area occupied by lipid droplets as well as a shift in the size distribution of these lipid droplets (Fig. 7). This is a very innovative outcome in unravelling NPL-induced steatosis. In addition to intestinal barrier and hepatic effects, we observed significant alterations of the gut microbiota, in particular at lower exposure doses. PS-NPL exposure induced a global decrease in alpha diversity and a clear shift in beta diversity in the CD0.1 and WD0.1 groups compared to their respective control groups, accompanied by changes in global microbial composition (Fig. 8 and 9). The effects observed under WD were less pronounced than those under CD, which can be explained by the strong impact of WD itself on the microbiota, already exerting a marked influence on microbial ecology. This pre-existing imbalance may saturate or constrain the microbiota's dynamic range, thereby limiting the detectability of additional compositional shifts induced by PS-NPL exposure. In this sense, NPL-induced changes might be more difficult to distinguish against an already highly perturbed baseline. It is also conceivable that subchronic WD exposure leads to increased ecological resilience in microbial communities. Repeated exposure to a diet rich in lipids and sugars exerts selective pressure favouring taxa that can tolerate oxidative and inflammatory environments.[68,69] Consequently, this adapted microbial ecosystem may be more stable when facing new challenges, such as PS-NPL exposure. As observed for the microbiota composition, significant metabolomic alterations were detected only in the CD0.1 group, with no clear changes under WD conditions. This attenuation likely reflects the dominant metabolic imprint of WD, which remodels gut microbial activity to a great extent.[70] Under these conditions, the metabolic profile may have stabilised or become saturated, thereby masking the subtle alterations induced by PS-NPL exposure. From the gut microbiota/mucus crosstalk perspective, our results indicate that PS-NPL exposure was accompanied by increases in sialylation of intestinal mucins, suggesting an adaptive remodelling of the mucosal barrier (Fig. 5K and L). While enhanced sialylation may initially improve mucus viscoelasticity and protection,[71] prolonged changes in glycosylation can disrupt host–microbe interactions and favour dysbiosis.[72] Increased sialylated substrates may benefit sialidase-expressing bacteria such as *Alloprevotella* and certain *Clostridia*, and indirectly *Lactobacillus*,[73,74] consistent with their increased abundance in CD0.1 mice. Conversely, butyrate producers like *Butyricicoccus* and *Eubacterium*, or non-sialidase species such as *Desulfovibrio* and *Oscillibacter*, decreased in CD0.1 and WD0.1 groups, possibly due to reduced ecological advantage. As altered mucin sialylation has also been linked to gut inflammation,[75] these findings raise concerns about long-term intestinal health. Moreover, as a probable consequence of gut microbiota alteration under CD0.1 conditions, we observed a reduction in caecal bile acids in CD0.1 mice (Fig. 10C). Further analysis is needed to determine which bile acid species are specifically affected; however, such a decrease has been associated with the onset of hepatic fibrosis and is known to impact gut–liver axis signalling.[76] These findings suggest that PS-NPL-induced intestinal dysbiosis could contribute to hepatic alterations by disrupting bile acid metabolism.

Conclusions

Taken together, our findings demonstrate that low-dose exposure to PS-NPLs can affect intestinal homeostasis, including microbial composition, barrier function, and local immune defence, with consequences extending to the liver. We showed that nutritional stress modulates the effects of NPLs, particularly in terms of the dose required to elicit biological changes. A key limitation of this study is that it only used male mice, which limits the generalisability of the findings and precludes an assessment of sex-specific responses. Indeed, hormonal status in females is known to influence drug metabolism,[77] immune function, and gut microbiota composition,[78,79] all of which could modulate the biological responses to NPL exposure. Moreover, the emerging evidence of sex-dependent differences in NPL toxicity[23,80,81] shows the need for future studies to include both sexes in order to provide a more comprehensive basis for human health risk assessment. We also emphasised that assessing the biological effects of NPLs requires consideration of their physicochemical behaviour, such as aggregation, interaction with dietary components, and transformation within the gastrointestinal environment. Another important point is that PS-NPLs used in this study were synthesised without any confounding additives. This demonstrates that toxicological effects can arise from the particulate form itself, in the absence of chemical substances. This is an important step forward in addressing the critical need to assess the health risks posed by NPLs, including human exposure data, for both healthy and at-risk populations. Given the prevalence of Western dietary habits, the interplay between diet, NPLs and gut health is of particular public health concern.

Author contributions

Conceptualization: MMB, SR. Data curation: CL, SM, MM, JJL, VB, CRM, MR, CC, MTF. Formal analysis: CL, SM, MM, VB, CB, RD, CRM, RL, JD, GDC, MR, CC, MTF, RG. Funding acquisition: MMB. Investigation: CL, SM, SR, BG, MR, JJL, CRM, RL, JD, MM, VB, CB, RD, HR. Methodology: MMB, SR, SM, BG, HR, CL, SM, VB, CB, HE. Supervision: MMB, SR, JJL, HR, HE. Validation: MMB, SR, JJL, HR, HE, CRM, MR, CC. Visualization, writing – original draft: CL, MR, SM, JJL, CRM, CC, MMB. Writing – review & editing: all authors.

Conflicts of interest

There are no conflicts to declare.

Data availability

The data supporting this article have been included as part of the supplementary information (SI). All illustrations have been created in BioRender: Eutamene, H. (2025).

Supplementary information: includes Fig. S1–S8 and detailed experimental procedures. See DOI: https://doi.org/10.1039/d5en00866b.

Acknowledgements

The authors wish to thank the National Research Institute for Agriculture, Food and Environment (INRAE, AlimH Division) for the PhD grant of C. Liebgott. The authors thank the French Agency for Food, Environmental and Occupational Health & Safety (ANSES) for financial support (NanoPlastX - No. EST-23-043). The authors would like to thank the TRI-Genotoul Imaging Platform (INRAE Auzeville Campus), the GeT-TriX Transcriptomics Platform (INRAE Saint-Martin du Touch Campus) and the EZOP Zootechnical Platform (INRAE Saint-Martin du Touch Campus).

Notes and references

1 Plastics – the fast Facts 2024 • Plastics Europe, https://plasticseurope.org/knowledge-hub/plastics-the-fast-facts-2024/, (accessed 26 May 2025).
2 R. C. Thompson, W. Courtene-Jones, J. Boucher, S. Pahl, K. Raubenheimer and A. A. Koelmans, Twenty years of microplastic pollution research-what have we learned?, *Science*, 2024, **386**, eadl2746.
3 J. Gigault, A. ter Halle, M. Baudrimont, P. Y. Pascal, F. Gauffre, T. L. Phi, H. El Hadri, B. Grassl and S. Reynaud, Current opinion: What is a nanoplastic?, *Environ. Pollut.*, 2018, **235**, 1030–1034.
4 L. Zimmermann, B. Geueke, L. V. Parkinson, C. Schür, M. Wagner and J. Muncke, Food contact articles as source of micro- and nanoplastics: a systematic evidence map, *npj Sci. Food*, 2025, **9**, 1–10.
5 C. Cella, R. La Spina, D. Mehn, F. Fumagalli, G. Ceccone, A. Valsesia and D. Gilliland, Detecting Micro-and Nanoplastics Released from Food Packaging: Challenges and Analytical Strategies, *Polymers*, 2022, **14**(6), 1238.
6 L. M. Hernandez, E. G. Xu, H. C. E. Larsson, R. Tahara, V. B. Maisuria and N. Tufenkji, Plastic Teabags Release Billions of Microparticles and Nanoparticles into Tea, *Environ. Sci. Technol.*, 2019, **53**, 12300–12310.
7 Y. Luo, C. T. Gibson, C. Chuah, Y. Tang, R. Naidu and C. Fang, Raman imaging for the identification of Teflon microplastics and nanoplastics released from non-stick cookware, *Sci. Total Environ.*, 2022, **851**(Pt 2), 158293.
8 Y. Chen, J. Shu, C. Li, X. Ye, Q. Li, C. George and J. Chen, Size Distribution of Micro-/Nanoplastic Particles and Their Chemical Speciation in the Atmosphere of Shanghai, China, *Environ. Sci. Technol.*, 2025, **59**, 12833–12842.
9 D. Materić, M. Peacock, J. Dean, M. Futter, T. Maximov, F. Moldan, T. Röckmann and R. Holzinger, Presence of nanoplastics in rural and remote surface waters, *Environ. Res. Lett.*, 2022, **17**(5), 054036.
10 A. Wahl, C. Le Juge, M. Davranche, H. El Hadri, B. Grassl, S. Reynaud and J. Gigault, Nanoplastic occurrence in a soil amended with plastic debris, *Chemosphere*, 2021, **262**, 127784.
11 N. Qian, X. Gao, X. Lang, H. Deng, T. M. Bratu, Q. Chen, P. Stapleton, B. Yan and W. Min, Rapid single-particle chemical imaging of nanoplastics by SRS microscopy, *Proc. Natl. Acad. Sci. U. S. A.*, 2024, **121**(3), e2300582121.
12 R. Lehner, C. Weder, A. Petri-Fink and B. Rothen-Rutishauser, Emergence of Nanoplastic in the Environment and Possible Impact on Human Health, *Environ. Sci. Technol.*, 2019, **53**(4), 1748–1765.
13 O. Keinänen, E. J. Dayts, C. Rodriguez, S. M. Sarrett, J. M. Brennan, M. Sarparanta and B. M. Zeglis, Harnessing PET to track micro- and nanoplastics in vivo, *Sci. Rep.*, 2021, **11**, 1–12.
14 S. Nikolic, M. Gazdic-Jankovic, G. Rosic, M. Miletic-Kovacevic, N. Jovicic, N. Nestorovic, P. Stojkovic, N. Filipovic, O. Milosevic-Djordjevic, D. Selakovic, M. Zivanovic, D. Seklic, N. Milivojević, A. Markovic, R. Seist, S. Vasilijic, K. M. Stankovic, M. Stojkovic and B. Ljujic, Orally administered fluorescent nanosized polystyrene particles affect cell viability, hormonal and inflammatory profile, and behavior in treated mice, *Environ. Pollut.*, 2022, **305**, 116206.
15 V. Stock, C. Laurisch, J. Franke, M. H. Dönmez, L. Voss, L. Böhmert, A. Braeuning and H. Sieg, Uptake and cellular effects of PE, PP, PET and PVC microplastic particles, *Toxicol. In Vitro*, 2021, **70**, 105021.
16 A. P. Walczak, P. J. M. Hendriksen, R. A. Woutersen, M. van der Zande, A. K. Undas, R. Helsdingen, H. H. J. van den Berg, I. M. C. M. Rietjens and H. Bouwmeester, Bioavailability and biodistribution of differently charged polystyrene nanoparticles upon oral exposure in rats, *J. Nanopart. Res.*, 2015, **17**, 1–13.
17 J. Qiao, R. Chen, M. Wang, R. Bai, X. Cui, Y. Liu, C. Wu and C. Chen, Perturbation of gut microbiota plays an important role in micro/nanoplastics-induced gut barrier dysfunction, *Nanoscale*, 2021, **13**, 8806–8816.
18 Y. He, Z. Li, T. Xu, D. Luo, Q. Chi, Y. Zhang and S. Li, Polystyrene nanoplastics deteriorate LPS-modulated duodenal permeability and inflammation in mice via ROS drived-NF-κB/NLRP3 pathway, *Chemosphere*, 2022, **307**, 135662.
19 L. Lu, Z. Wan, T. Luo, Z. Fu and Y. Jin, Polystyrene microplastics induce gut microbiota dysbiosis and hepatic lipid metabolism disorder in mice, *Sci. Total Environ.*, 2018, **631–632**, 449–458.
20 C. Shi, X. Han, W. Guo, Q. Wu, X. Yang, Y. Wang, G. Tang, S. Wang, Z. Wang, Y. Liu, M. Li, M. Lv, Y. Guo, Z. Li, J. Li, J. Shi, G. Qu and G. Jiang, Disturbed Gut-Liver axis indicating oral exposure to polystyrene microplastic potentially increases the risk of insulin resistance, *Environ. Int.*, 2022, **164**, 107273.
21 B. Liang, X. Huang, Z. Li, Y. Huang, Y. Deng, X. Chen, Y. Zhong, X. Yang, Y. Feng, R. Bai, B. Fan, H. Xian, H. Li, S. Tang and Z. Huang, Polystyrene nanoplastics trigger ferroptosis in Nrf2-deficient gut via ether phospholipid accumulation, *Environ. Int.*, 2025, **197**, 109367.

22 J. Dong, F. Yang, Y. Xu, Q. Zhao, X. Li, T. Liu and Y. Tang, Exploring the Mechanism of Kidney Injury in Mice Induced by High-Fat Diet and Polystyrene Nanoplastics Co-Exposure Through the Kidney-Gut Axis, *J. Agric. Food Chem.*, 2025, **73**, 17956–17966.
23 J. Tang, W. Bu, W. Hu, Z. Zhao, L. Liu, C. Luo, R. Wang, S. Fan, S. Yu, Q. Wu, X. Wang and X. Zhao, Ferroptosis Is Involved in Sex-Specific Small Intestinal Toxicity in the Offspring of Adult Mice Exposed to Polystyrene Nanoplastics during Pregnancy, *ACS Nano*, 2023, **17**, 2440–2449.
24 B. Du, T. Li, H. He, X. Xu, C. Zhang, X. Lu, Y. Wang, J. Cao, Y. Lu, Y. Liu, S. Hu, J. Li, L. Li and M. Shi, Analysis of Biodistribution and in vivo Toxicity of Varying Sized Polystyrene Micro and Nanoplastics in Mice, *Int. J. Nanomed.*, 2024, **19**, 7617–7630.
25 J. Huang, X. Sun, Y. Wang, J. Su, G. Li, X. Wang, Y. Yang, Y. Zhang, B. Li, G. Zhang, J. Li, J. Du, R. H. Nanjundappa, C. S. Umeshappa and K. Shao, Biological interactions of polystyrene nanoplastics: Their cytotoxic and immunotoxic effects on the hepatic and enteric systems, *Ecotoxicol. Environ. Saf.*, 2023, **264**, 115447.
26 Y. Y. Lu, L. Lu, H. Y. Ren, W. Hua, N. Zheng, F. Y. Huang, J. Wang, M. Tian and Q. Huang, The size-dependence and reversibility of polystyrene nanoplastics-induced lipid accumulation in mice: Possible roles of lysosomes, *Environ. Int.*, 2024, **185**, 108532.
27 B. Bolon and W. M. Haschek, The Exposome in Toxicologic Pathology, *Toxicol. Pathol.*, 2020, **48**, 718–720.
28 Y. Wang, Z. Wei, K. Xu, X. Wang, X. Gao, Q. Han, S. Wang and M. Chen, The effect and a mechanistic evaluation of polystyrene nanoplastics on a mouse model of type 2 diabetes, *Food Chem. Toxicol.*, 2023, **173**, 113642.
29 S. Tian, R. Li, J. Li and J. Zou, Polystyrene nanoplastics promote colitis-associated cancer by disrupting lipid metabolism and inducing DNA damage, *Environ. Int.*, 2025, **195**, 109258.
30 L. Li, M. Xu, C. He, H. Wang and Q. Hu, Polystyrene nanoplastics potentiate the development of hepatic fibrosis in high fat diet fed mice, *Environ. Toxicol.*, 2022, **37**, 362–372.
31 H. T. Shiu, X. Pan, Q. Liu, K. Long, K. K. Y. Cheng, B. C.-B. Ko, J. K.-H. Fang and Y. Zhu, Dietary exposure to polystyrene nanoplastics impairs fasting-induced lipolysis in adipose tissue from high-fat diet fed mice, *J. Hazard. Mater.*, 2022, **440**, 129698.
32 C. Liebgott, I. Chaib, P. Doyen, H. Robert, H. Eutamene, G. Duflos, S. Reynaud, B. Grassl and M. Mercier-Bonin, Fate and impact of nanoplastics in the human digestive environment after oral exposure: A common challenge for toxicology and chemistry, *TrAC, Trends Anal. Chem.*, 2023, **166**, 117175.
33 O. Pikuda, E. G. Xu, D. Berk and N. Tufenkji, Toxicity Assessments of Micro- and Nanoplastics Can Be Confounded by Preservatives in Commercial Formulations, *Environ. Sci. Technol. Lett.*, 2019, **6**, 21–25.
34 J. B. J. Kamphuis, M. Mercier-Bonin, H. Eutamène and V. Theodorou, Mucus organisation is shaped by colonic content; A new view, *Sci. Rep.*, 2017, **7**, 8527.
35 J. Schindelin, I. Arganda-Carreras, E. Frise, V. Kaynig, M. Longair, T. Pietzsch, S. Preibisch, C. Rueden, S. Saalfeld, B. Schmid, J. Y. Tinevez, D. J. White, V. Hartenstein, K. Eliceiri, P. Tomancak and A. Cardona, Fiji: An open-source platform for biological-image analysis, *Nat. Methods*, 2012, **9**, 676–682.
36 J. J. Godon, E. Zumstein, P. Dabert, F. Habouzit and R. Moletta, Molecular microbial diversity of an anaerobic digestor as determined by small-subunit rDNA sequence analysis, *Appl. Environ. Microbiol.*, 1997, **63**, 2802–2813.
37 R. Schmieder and R. Edwards, Quality control and preprocessing of metagenomic datasets, *Bioinformatics*, 2011, **27**, 863–864.
38 T. Magoč and S. L. Salzberg, FLASH: fast length adjustment of short reads to improve genome assemblies, *Bioinformatics*, 2011, **27**, 2957–2963.
39 T. Rognes, T. Flouri, B. Nichols, C. Quince and F. Mahé, VSEARCH: A versatile open source tool for metagenomics, *PeerJ*, 2016, **4**, e2584.
40 R. C. Edgar, B. J. Haas, J. C. Clemente, C. Quince and R. Knight, UCHIME improves sensitivity and speed of chimera detection, *Bioinformatics*, 2011, **27**, 2194–2200.
41 F. Escudié, L. Auer, M. Bernard, M. Mariadassou, L. Cauquil, K. Vidal, S. Maman, G. Hernandez-Raquet, S. Combes and G. Pascal, FROGS: Find, Rapidly, OTUs with Galaxy Solution, *Bioinformatics*, 2018, **34**, 1287–1294.
42 Q. Wang, G. M. Garrity, J. M. Tiedje and J. R. Cole, Naïve Bayesian classifier for rapid assignment of rRNA sequences into the new bacterial taxonomy, *Appl. Environ. Microbiol.*, 2007, **73**, 5261–5267.
43 M. Bernard, O. Rué, M. Mariadassou and D. Pascal, FROGS: a powerful tool to analyse the diversity of fungi with special management of internal transcribed spacers, *Briefings Bioinf.*, 2021, **22**(6), bbab318.
44 R. H. Nilsson, K. H. Larsson, A. F. S. Taylor, J. Bengtsson-Palme, T. S. Jeppesen, D. Schigel, P. Kennedy, K. Picard, F. O. Glöckner, L. Tedersoo, I. Saar, U. Kõljalg and K. Abarenkov, The UNITE database for molecular identification of fungi: Handling dark taxa and parallel taxonomic classifications, *Nucleic Acids Res.*, 2019, **47**, D259–D264.
45 N. Segata, J. Izard, L. Waldron, D. Gevers, L. Miropolsky, W. S. Garrett and C. Huttenhower, Metagenomic biomarker discovery and explanation, *Genome Biol.*, 2011, **12**(6), R60.
46 C. Martias, N. Baroukh, S. Mavel, H. Blasco, A. Lefèvre, L. Roch, F. Montigny, J. Gatien, L. Schibler, D. Dufour-Rainfray, L. Nadal-Desbarats and P. Emond, Optimization of Sample Preparation for Metabolomics Exploration of Urine, Feces, Blood and Saliva in Humans Using Combined NMR and UHPLC-HRMS Platforms, *Molecules*, 2021, **26**, 4111.
47 K. Gillois, C. Rivard, C. Levasseur-garcia, V. Bezirard, H. Terrisse, R. Leonard, C. Robbe-masselot, E. Maguin, M. L. Richard, V. Theodorou, M. Ropers, M. Mercier-bonin and H.

Robert, Environmental Science Nano food nanotoxicology, *Environ. Sci.: Nano*, 2023, **10**, 902–921.

48 A. M. Ghaleb, B. B. McConnell, K. H. Kaestner and V. W. Yang, Altered intestinal epithelial homeostasis in mice with intestine-specific deletion of the Krüppel-like factor 4 gene, *Dev. Biol.*, 2011, **349**, 310–320.

49 E. Guaní-Guerra, T. Santos-Mendoza, S. O. Lugo-Reyes and L. M. Terán, Antimicrobial peptides: General overview and clinical implications in human health and disease, *Clin. Immunol.*, 2010, **135**, 1–11.

50 B. Chassaing, G. Srinivasan, M. A. Delgado, A. N. Young, A. T. Gewirtz and M. Vijay-Kumar, Fecal Lipocalin 2, a Sensitive and Broadly Dynamic Non-Invasive Biomarker for Intestinal Inflammation, *PLoS One*, 2012, **7**, e44328.

51 B. O. Schroeder, G. M. H. Birchenough, M. Ståhlman, L. Arike, M. E. V. Johansson, G. C. Hansson and F. Bäckhed, Bifidobacteria or fiber protect against diet-induced microbiota-mediated colonic mucus deterioration, *Cell Host Microbe*, 2017, **23**, 27.

52 S. Singh and R. R. Tiwari, Micro/nanoplastics and human health: A review of the evidence, consequences, and toxicity assessment, *Food Chem. Toxicol.*, 2025, **203**, 115595.

53 C. R. S. de Oliveira, G. Maestri, G. A. Tochetto, J. L. de Oliveira, E. Stiegelmaier, T. V. Fischer and A. P. S. Immich, Nanoplastics: Unveiling Contamination Routes and Toxicological Implications for Human Health, *Curr. Anal. Chem.*, 2024, **21**, 175–190.

54 S. Snipstad, S. Hak, H. Baghirov, E. Sulheim, Ý. Mørch, S. Lélu, E. von Haartman, M. Bäck, K. P. R. Nilsson, A. S. Klymchenko, C. de Lange Davies and A. K. O. Åslund, Labeling nanoparticles: Dye leakage and altered cellular uptake, *Cytometry, Part A*, 2017, **91**, 760–766.

55 M. Al-Sid-Cheikh, S. J. Rowland, R. Kaegi, T. B. Henry, M. A. Cormier and R. C. Thompson, Synthesis of 14C-labelled polystyrene nanoplastics for environmental studies, *Commun. Mater.*, 2020, **1**(1), 97.

56 T. Staufer, V. Kopatz, A. Pradel, T. Brodie, R. Kuhrwahl, D. Stroka, J. Wallner, L. Kenner, V. Pichler, F. Grüner and D. M. Mitrano, Biodistribution of nanoplastics in mice: advancing analytical techniques using metal-doped plastics, *Commun. Biol.*, 2025, **8**, 1–13.

57 R. Danquigny, B. Grassl, J. Jiménez-Lamana, M. Metian, S. Le Faucheur, F. Oberhaensli, K. Sdiri, K. Mattsson, P. Jame, A. Anchisi, E. Bonjour and S. Reynaud, 13C-labeled nanoplastic model materials: Synthesis and evaluation of their use in ecotoxicology through bioaccumulation studies in aquatic crustaceans, *J. Hazard. Mater.*, 2025, **495**, 138810.

58 T. T. Huong Do, P. Hindlet, A. J. Dupriet-Waligora, N. Kapel, N. Neveux, V. Mignon, C. Deloménie, R. Farinotti, B. Fève and M. Buyse, Disturbed intestinal nitrogen homeostasis in a mouse model of high-fat diet-induced obesity and glucose intolerance, *Am. J. Physiol.*, 2014, **306**, 668–680.

59 M. B. Paul, L. Böhmert, A. F. Thünemann, K. Loeschner, L. Givelet, C. Fahrenson, A. Braeuning and H. Sieg, Influence of artificial digestion on characteristics and intestinal cellular effects of micro-, submicro- and nanoplastics, *Food Chem. Toxicol.*, 2024, **184**, 114423.

60 C. H. Lee and J. K. H. Fang, Effects of temperature and particle concentration on aggregation of nanoplastics in freshwater and seawater, *Sci. Total Environ.*, 2022, **817**, 152562.

61 G. M. DeLoid, X. Cao, D. Bitounis, D. Singh, P. M. Llopis, B. Buckley and P. Demokritou, Toxicity, uptake, and nuclear translocation of ingested micro-nanoplastics in an in vitro model of the small intestinal epithelium, *Food Chem. Toxicol.*, 2021, **158**, 112609.

62 V. Stock, L. Böhmert, G. Coban, G. Tyra, M. L. Vollbrecht, L. Voss, M. B. Paul, A. Braeuning and H. Sieg, Microplastics and nanoplastics: Size, surface and dispersant – What causes the effect?, *Toxicol. In Vitro*, 2022, **80**, 105314.

63 H. Tan, T. Yue, Y. Xu, J. Zhao and B. Xing, Microplastics Reduce Lipid Digestion in Simulated Human Gastrointestinal System, *Environ. Sci. Technol.*, 2020, **54**, 12285–12294.

64 G. Łazarski, N. Rajtar, M. Romek, D. Jamróz, M. Rawski and M. Kepczynski, Interaction of Polystyrene Nanoplastic with Lipid Membranes, *J. Phys. Chem. B*, 2025, **129**, 4110–4122.

65 Y. Y. Lu, L. Lu, H. Y. Ren, W. Hua, N. Zheng, F. Y. Huang, J. Wang, M. Tian and Q. Huang, The size-dependence and reversibility of polystyrene nanoplastics-induced lipid accumulation in mice: Possible roles of lysosomes, *Environ. Int.*, 2024, **185**, 108532.

66 T. Okamura, M. Hamaguchi, Y. Hasegawa, Y. Hashimoto, S. Majima, T. Senmaru, E. Ushigome, N. Nakanishi, M. Asano, M. Yamazaki, R. Sasano, Y. Nakanishi, H. Seno, H. Takano and M. Fukui, Oral Exposure to Polystyrene Microplastics of Mice on a Normal or High-Fat Diet and Intestinal and Metabolic Outcomes, *Environ. Health Perspect.*, 2023, **131**, 27006.

67 M. S. Winzell and B. Ahrén, The High-Fat Diet–Fed MouseA Model for Studying Mechanisms and Treatment of Impaired Glucose Tolerance and Type 2 Diabetes, *Diabetes*, 2004, **53**, S215–S219.

68 C. Zhang, M. Zhang, X. Pang, Y. Zhao, L. Wang and L. Zhao, Structural resilience of the gut microbiota in adult mice under high-fat dietary perturbations, *ISME J.*, 2012, **6**, 1848–1857.

69 S. K. Dogra, J. Doré and S. Damak, Gut Microbiota Resilience: Definition, Link to Health and Strategies for Intervention, *Front. Microbiol.*, 2020, **11**, 572921.

70 A. Agus, J. Denizot, J. Thévenot, M. Martinez-Medina, S. Massier, P. Sauvanet, A. Bernalier-Donadille, S. Denis, P. Hofman, R. Bonnet, E. Billard and N. Barnich, Western diet induces a shift in microbiota composition enhancing susceptibility to Adherent-Invasive E. coli infection and intestinal inflammation, *Sci. Rep.*, 2016, **6**, 1–14.

71 A. Weston, S. C. Vladescu, T. Reddyhoff, A. Griffiths, T. Crouzier, M. Fielden, J. A. Garnett and G. H. Carpenter, The influence of ions on the lubricative abilities of mucin and the role of sialic acids, *Colloids Surf., B*, 2023, **227**, 113327.

72 M. Taniguchi, R. Okumura, T. Matsuzaki, A. Nakatani, K. Sakaki, S. Okamoto, A. Ishibashi, H. Tani, M. Horikiri, N.

Kobayashi, H. Y. Yoshikawa, D. Motooka, D. Okuzaki, S. Nakamura, T. Kida, A. Kameyama and K. Takeda, Sialylation shapes mucus architecture inhibiting bacterial invasion in the colon, *Mucosal Immunol.*, 2023, **16**, 624–641.

73 N. Juge, L. Tailford and C. D. Owen, Sialidases from gut bacteria: A mini-review, *Biochem. Soc. Trans.*, 2016, **44**, 166–175.

74 P. Pelayo, F. A. Hussain, C. A. Werlang, C. M. Wu, B. M. Woolston, C. M. Xiang, L. Rutt, M. T. France, J. Ravel, K. Ribbeck, D. S. Kwon and E. P. Balskus, Prevotella are major contributors of sialidases in the human vaginal microbiome, *Proc. Natl. Acad. Sci. U. S. A.*, 2024, **121**, e2400341121.

75 X. Ma, M. Li, X. Wang, G. Qi, L. Wei and D. Zhang, Sialylation in the gut: From mucosal protection to disease pathogenesis, *Carbohydr. Polym.*, 2024, **343**, 122471.

76 H. Xiang, Z. Liu, H. Xiang, D. Xiang, S. Xiao, J. Xiao, W. Shen, P. Hu, H. Ren and M. Peng, Dynamics of the gut-liver axis in rats with varying fibrosis severity, *Int. J. Biol. Sci.*, 2022, **18**, 3390–3404.

77 D. J. Waxman and M. G. Holloway, Sex differences in the expression of hepatic drug metabolizing enzymes, *Mol. Pharmacol.*, 2009, **76**, 215–228.

78 M. Elderman, F. Hugenholtz, C. Belzer, M. Boekschoten, A. van Beek, B. de Haan, H. Savelkoul, P. de Vos and M. Faas, Sex and strain dependent differences in mucosal immunology and microbiota composition in mice, *Biol. Sex Differ.*, 2018, **9**, 1–18.

79 P. Shobeiri, A. Kalantari, A. L. Teixeira and N. Rezaei, Shedding light on biological sex differences and microbiota–gut–brain axis: a comprehensive review of its roles in neuropsychiatric disorders, *Biol. Sex Differ.*, 2022, **13**, 1–24.

80 X. Chen, S. Huang, L. Wang, K. Liu and H. Wu, Maternal exposure to polystyrene nanoplastics induces sex-specific cardiotoxicity in offspring mice, *Heliyon*, 2024, **10**, e39139.

81 X. Chen, L. Wang, K. Liu, Q. Wang, R. Li, L. Niu and H. Wu, Maternal exposure to polystyrene nanoplastics induces sex-specific kidney injury in offspring, *Ecotoxicol. Environ. Saf.*, 2025, **293**, 118006.